Sand bars in tidal channels
Part 2. Tidal meanders

By L. SOLARI[1]†, G. SEMINARA[1], S. LANZONI[2], M. MARANI[2] AND A. RINALDO[2]

[1]Dipartimento di Ingegneria Ambientale, Università di Genova,
Via Montallegro 1, 16145 Genova, Italy
e-mail: sem@diam.unige.it

[2]Dipartimento di Ingegneria Idraulica, Marittima e Geotecnica,
Università di Padova, via Loredan 20, 35131 Padova, Italy
e-mail: rinaldo@idra.unipd.it

Careful analysis of new field observations on the geometry of meandering tidal channels reveals that the values of meander wavelengths as well as curvatures, conveniently scaled by local channel width, fall within a fairly restricted range, suggesting the existence of some mechanistic process controlling meander formation. A three-dimensional model is then proposed to predict flow and bed topography in weakly meandering tidal channels. The analysis is developed for meander wavelengths much smaller than the tidal wavelength and assuming that sediment is transported both as bedload and as suspended load. Both conditions are typically met in nature. Due to the symmetry of the meander pattern investigated, the theory indicates that oscillations associated with the basic flow give rise to symmetric oscillations of the point bar–pool pattern around the locations of maximum curvature. However, no net migration in a tidal cycle is present, at least for periodic tides with zero mean. Suspended load leads both to an enhanced bottom deformation and to a downstream shifting of the position of the point bar. The model then provides the basis of a planimetric instability theory of the type developed for river meanders (Blondeaux & Seminara 1985). Though the available data do not yet allow a detailed quantitative comparison, it is shown that the wavelengths selected by the 'bend mechanism' are somewhat larger than those typically encountered in nature. The geomorphology of the process of meander formation in tidal environments is then discussed and, upon comparison with observational evidence, points out the need for various developments of the present model.

1. Introduction

The process of meandering of tidal channels is relatively unexplored in spite of the fact that meandering is a ubiquitous feature of tidal networks both in estuaries and in lagoons (see figure 1). We report in §2 some very recent observational evidence which clearly shows that meander wavelength scales with channel width, thus suggesting that the process of meander formation must arise from the effect of secondary flows driven by some planimetric instability somewhat similar to that occurring in the

† Present address: Dipartimento di Ingegneria Civile, Università di Firenze, Via S. Marta 3, 50139 Firenze, Italy; e-mail: Luca.Solari@dicea.unifi.it.

fluvial case. Indeed, a considerable amount of knowledge has been established in the last two decades on the simpler, yet fundamental, problem of river meandering. In particular we know that meandering alluvial rivers are typically characterized by the formation of a sequence of so called point bars, i.e. regions located along the inner (convex) banks where sediments accumulate. Correspondingly, along the outer (concave) banks pools form close to the bend apexes. These alternate sequences of pools and bars are essentially steady, i.e. they propagate at the very slow time scale associated with the planimetric evolution of the meandering pattern with migration speeds of the order of metres per year, unlike the alternate bar pattern typically observed in straight channels which migrates downstream with a speed of the order of metres per hour.

The basic mechanisms controlling the formation of the point-bar–pool pattern have been clarified through the work of several researchers, starting from the pioneering contributions of Rozovskij (1957) and Engelund (1974) (see Ikeda & Parker 1989). It is now fairly well established that the lateral bed slope associated with the bar–pool pattern of meander bends is maintained through the development of a secondary flow which acts on sediment particles.

In a constant curvature channel, sufficiently far from the bend entrance for the flow and bed topography to be fully developed (i.e. uniform in the longitudinal direction), the secondary flow is centrifugally driven: more precisely it arises from the inability of the lateral pressure gradient associated with the lateral slope of the free surface to balance the effective centrifugal force acting on fluid particles, the former being constant in the vertical direction while the latter increases upwards. The resulting secondary flow is constrained by continuity to have vanishing depth average, directed inwards close to the bed where the pressure gradient exceeds the centrifugal force and outwards close to the free surface. Similarly, sediment continuity constrains the lateral component of bedload transport to vanish. Hence, a delicate balance arises between two lateral forces acting on sediment particles moving as bedload: the inward directed lateral component of the drag force associated with the effect of the secondary flow; and the outward directed lateral component of particle weight. Equilibrium is achieved for a lateral slope which increases slightly in the outward direction, giving rise to deposition at the inner bend and scour at the outer bend.

The occurrence of longitudinal variations of channel curvature complicates the above picture. In fact continuity now forces an additional and often dominant, topographically driven, component of secondary flow which has a non-vanishing depth average and transfers longitudinal momentum from each pool to the next one, leading to a thread of high velocity winding through the channel. Moreover, a lateral component of the bedload transport vector originates from the longitudinal variations of the longitudinal component of bedload transport. In order to allow for this lateral component of bedload transport an additional contribution to the lateral slope is required. It turns out to be out of phase relative to curvature, and the phase lag of the bar–pool pattern depends on meander wavenumber for given flow and sediment characteristics.

The presence of a significant fraction of sediments transported in suspension adds further contributions to the above balance as both the centrifugal and the topographical components of the secondary flow advect suspended sediments, giving rise to additional lateral sediment fluxes. However the resulting bar–pool pattern does not change qualitatively.

In the present paper we wish to extend the above framework to the tidal environment. More precisely, we intend to determine the flow pattern and the bed topography
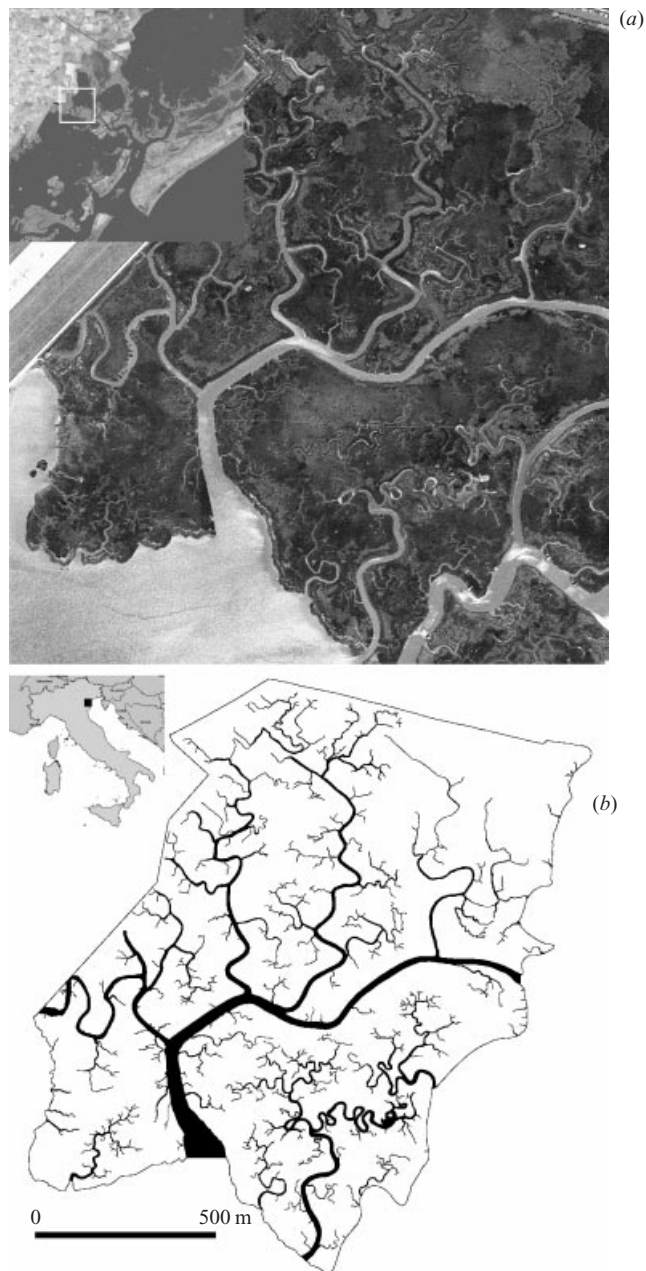
FIGURE 1. Typical tidal meanders, developed within the landforms of the lagoon of Venice (Italy). On the central inset showing Italy the black square indicates (roughly) the inset of (*a*) in the upper left corner, which shows, from remote imaging, a detail of the northern lagoon of Venice, termed Palude Pagliaga. The main part of (*a*) is an enlargement of the squared zone in the upper inset, showing the geomorphological patterns typically encountered within a mesotidal saltmarsh, with drainage-like features and a fully developed dendritic structure defining the tidal network. Here we emphasize a comparison between the remotely sensed image of the network of meandering tidal creeks (*a*) and the related automatic channel identification (*b*) from digital terrain maps, proposed by Fagherazzi *et al.* (1999). Notice the obvious similarity of imaged and synthetic landforms, the richness of the patterns observed and the rather different features of meanders even in adjacent zones.

in tidal meandering channels. The distinct novel feature of such problem is the unsteady periodic character of the basic flow which reverses direction at each half-cycle. Note that we are implicitly assuming that the landscape forming events are due to astronomical tides; meteorologically dominated tides are excluded from the present model. The present analysis is equipped to deal with any periodic tide, though for the sake of simplicity results will be presented only for a purely harmonic tide. As a result of unsteadiness, it will appear that the bar–pool pattern also oscillates in time. The analysis will be carried on for regularly meandering channels such that the meander wavelength is much smaller than the tidal wavelength, a condition typical of both estuarine and lagoon environments. Under these conditions, just like in the case of tidal free bars treated in Part 1 of the present paper (Seminara & Tubino 2001), the basic state is slowly varying in space at the bar scale and a local analysis is appropriate at the leading order of approximation. Moreover, provided local inertia is small enough with respect to other relevant effects (as already discussed in Part 1), a similarity solution exists which is only parametrically dependent on time.

The knowledge of flow and bed topography in meandering channels allows one to investigate the problem of meander formation in tidal channels. The origin of meandering is a subject which has been of great interest in the classical river case. Two main theories have been put forward in the recent literature: they are known as bar theory and bend theory of river meandering. The former approach, which may perhaps be traced back to Leopold & Wolman (1957), essentially assumes that alternate bars, i.e. free migrating modes excited by a bottom instability, are precursors of meanders: in other words the presence of alternate bars in the originally straight channel would be the triggering mechanism which forces bank erosion, hence meander wavelength would coincide with bar wavelength. On the other hand the bend approach, originally proposed by Ikeda, Parker & Sawai (1981), assumes that bank erosion originates from steady flow perturbations induced by channel curvature, i.e. from forced modes rather than from migrating free alternate bar modes, hence the wavelength selected by the process of meandering initiation should be such as to maximize curvature-induced flow and topography perturbations. Blondeaux & Seminara (1985) have clarified the relationship between bar and bend theories, showing that the bend theory selects a particular free bar mode which neither grows nor migrates, i.e. the bend approach may be considered just a particular case of the bar approach. Moreover, it turns out that, under admittedly idealized conditions consisting of the occurrence of specific values of meander wavenumber and width to depth ratio for given flow and sediment characteristics, curvature forces a natural solution of the flow–cohesionless bed system leading to the occurrence of resonance, displayed by the presence of an infinite peak in the response of flow and bed topography at least in the context of a linearized theoretical framework. Meanders thus behave like resonators, displaying all the linear and nonlinear features of such mechanical systems, as clearly shown by Seminara & Tubino (1992). In practice resonance never occurs but the peak of bend theories is clearly related to the occurrence of quasi-resonant conditions. An approach related to that of Blondeaux & Seminara (1985) was independently pursued by Struiksma *et al.* (1985) who concentrated their attention on the role of spatial rather than temporal modes: in other words they showed that, along with spatially periodic and temporally growing migrating bar modes, the flow–cohesionless bed system allows for the existence of spatially damped oscillatory bar modes which neither amplify in time nor migrate. The resonant mode of Blondeaux & Seminara (1985) is just that particular spatial mode which neither grows nor amplifies in space.

Comparison of theories with experimental observations is not conclusive because

reproducing the process of meandering initiation in the laboratory is quite hard while field observations cannot be performed under clearly controlled conditions. The current state of the art, however, seems to favour the idea that spatial rather than temporal modes control meander formation in the fluvial environment. In the tidal environment the picture is somewhat altered by the fact that, as shown in Part 1, free modes do not exhibit a net migration in a tidal cycle. Hence free modes might be the triggering perturbations which force the planimetric evolution of the channel. However, an extension of the theory of Blondeaux & Seminara (1985) to the present tidal configuration reveals that a bend instability mechanism may indeed also operate for tidal channels and selects wavenumbers which are smaller than the wavenumbers of free bars. On the contrary the latter wavenumbers fall in the stable range of meander wavenumbers, hence a bar mechanism does not seem to be a feasible explanation of the process of meander formation in tidal environments, at least in the context of a linear theory. Observational evidence, especially remotely gathered and objectively manipulated, is also available (Langbein 1963; Pestrong 1965; Allen & Pye 1992; French & Stoddard 1992; Steel & Pye 1997; Fagherazzi *et al.* 1999; Rinaldo *et al.* 1999*a,b*). A method of automatic extraction of tidal channels from topographic data of marshes and tidal flats has recently allowed new and quantitative descriptions of tidal landforms over a wide range of scales. Coupled with data on the hydrodynamics such observations will eventually yield the benchmark against which to compare theoretical assumptions and results. At present, as discussed in §2, available data concern only the geometry of tidal meandering channels. This allows some qualitative comparison with theoretical results, which suggests that theory captures the correct order of magnitude of meander wavenumber, but it systematically overpredicts meander wavelengths. Hence, we cannot claim that the present work conclusively proves that a bend mechanism is responsible for the formation of tidal meanders.

The procedure followed in the rest of the paper is as follows. After a section on new observational evidence we extend the mathematical formulation proposed in Part 1 to the meandering configuration examined herein. This formulation is linearized in §4 where we also derive the linear solution for flow and bed topography in meandering tidal channels, the results being presented in §5. The previous findings allow us to test the performance of a bend approach as opposed to a bar approach to the problem of meandering initiation. This test is performed in §6 while some conclusions follow in §7.

2. Observational evidence

Through a recent method for automatic extraction of a tidal network from topographic fields (Fagherazzi *et al.* 1999; Rinaldo *et al.* 1999*a,b*), we analyse the morphology of meandering patterns that we observe in nature in different tidal environments (e.g. figure 1). Specifically, we measure widths, wavelengths and sinuousities (that is, a range of planimetric measures) from digital maps of the imprinting of planar patterns of the channel network. Figure 1 shows an example of such an extraction for a region of the northern lagoon of Venice, whose climatic, geologic and vegetational features are described in the above references. Other available patterns, also described therein, are in the Barnstable lagoon (MA, USA) and the Petaluma estuary of the bay of San Francisco (CA, USA) as it appears from detailed maps from the beginning of the century.

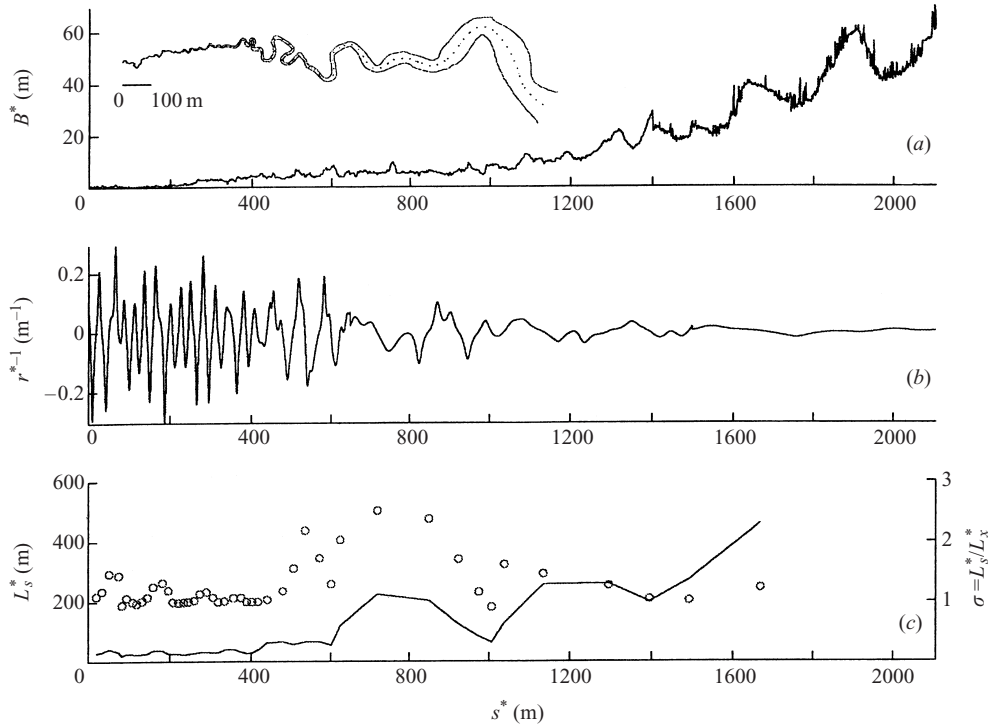The extraction method discriminates among topographic elevations and curvatures

FIGURE 2. An example of raw, dimensional observational data from tidal meanders: (*a*) As an inset, the planimetric development of a tidal meander is shown by its centreline (dotted) and the sidelines (solid). The graph shows the measured planimetric evolution of the channel width within two orders of magnitude from the order of 1 m to the order of 100 m. The width is plotted against the curvilinear coordinate with origin at the left end of the meandering pattern, and is gauged by the digital terrain map manipulation described in Rinaldo *et al.* (1999); (*a, b*) planimetric evolution of the curvature $r^{*-1}(s^*)$ as described in the text; (*c*) planimetric evolution of the intrinsic wavelength of the meanders (L_s^*, solid line, left scale) and the related sinuosity (L_s^*/L_x^*) (dotted line, right scale).

to devise a reliable automatic map of connected channelized features of the topographic landscape. As such, it employs discrete units of landscape (i.e. pixels), typically of the order of few metres, depending on the accuracy of the digital topographic basis. It should be emphasized, therefore, that small cross-sections (of finer scale than the pixel size) cannot be considered reliably identified by the method. Nevertheless, it is quite interesting to observe (e.g. figure 2), that widths grow rapidly to orders of one hundred metres in many cases of interest, thereby allowing precise quantitative descriptions for most sites.

Figure 2 shows a complete set of planimetric measures for a meander within the Pagliaga region shown in figure 1, specifically: width, curvature, wavelength and sinuosity development along the intrinsic coordinate defined by the channel centreline *s*. The planimetric development of channel width, say $2B^*(s^*)$, where a star denotes a dimensional quantity subsequently made dimensionless (for notation, see Part 1, §2), is identified through the automatic procedures described in Fagherazzi *et al.* (1999). We also compute local curvatures $r^{*-1}(s^*)$ of the channel centreline. Curvatures, known to play a central role in meander geometry (e.g. Langbein & Leopold 1964), are generally determined on the basis of the intrinsic curve defined by the angle $\vartheta(s^*)$ formed by the local tangent of the centreline at s^* with a fixed reference axis.

Curvatures are then defined as $r^{*-1}(s^*) = -\mathrm{d}\vartheta/\mathrm{d}s^*$. A discrete Fourier transform of the map of the coordinates $x(s^*), y(s^*)$ of the centreline is suitably analysed involving appropriate windowing techniques which allow a spectral representation of the $\vartheta(s^*)$ curve that can be analytically differentiated, owing to its basic regularities, to yield reliable curvatures (figure 2*b*). Details on signal processing techniques are in Zandolin (1999). We also measure directly intrinsic (L_s^*) and locally Cartesian (L_x^*) wavelengths of the tidal meanders (figure 2*c*), and their ratio defined as the sinuosity σ. Intrinsic wavelengths L_s^* are distances between adjacent inflection points on a map computed along the intrinsic coordinate s^*. Local Cartesian analogues L_x^* define the same measure computed along a fixed Cartesian axis, and obviously mimic the above when curvatures are small and the total length of the meandering reach divided by its projection on the reference axis approaches the unit value. Note that the most reliable procedure for the automatic identification of the inflection point is the location of zeros of the curvatures after spectral approximations and appropriate windowing (see caption of figure 2 for further details).

Figure 3 shows a synthesis of our observational results. There we have plotted data pertaining the dimensionless ratio of (intrinsic) wavelengths to channel widths from source to outlet of a number of tidal meanders. Note that the typical, and surprisingly robust, range of values is about $2\pi B^*/L_s^* \sim 0.2$–0.4. The above range is reproduced well in quite different tidal environments. Figure 4 shows a plot of the spatial development of the dimensionless product of local curvature and half-width, $r^{*-1}(s^*)B^*(s^*)$, for three tidal meanders of different size and geographic location. It is interesting to observe the fluctuating patterns shown by all the gauges, where nevertheless the product maintains a remarkably constant mean despite at least one order of magnitude change in the half-width (say, from a few metres to about 100 metres).

Though incomplete for a conclusive comparison with theory, owing to the lack of detailed information about the sediment properties relevant to transport mechanisms and about the features of landforming hydrodynamics, we nevertheless provide valuable empirical elements, especially planar features, for the theory of tidal meanders which we elaborate in the ensuing discussion.

3. Formulation of the problem

Let us consider a long meandering channel connected at some initial cross-section with a tidal sea (figure 5). Except for its meandering character the geometry of the channel is otherwise taken to be identical to that described in the companion paper (Part 1) to which we refer the reader for notation. For the moment we assume the banks to be non-erodible, an assumption that will be relaxed in §6. Moreover, for the sake of simplicity, we assume that the curvature of the channel axis undergoes periodic oscillations described by the classical Langbein & Leopold (1964) sine generated curve. This assumption is by no means crucial, the theory developed herein being amenable to a relative straightforward generalization to an arbitrary, albeit slowly varying, curvature distribution. Hence we assume

$$r^{*-1} = R_0^{*-1}(\exp i\lambda^* s^* + \text{c.c.}), \tag{3.1}$$

where $r^*(s^*)$ is the local radius of curvature of the channel axis, R_0^* is twice the radius of curvature at the bend apex, λ^* is meander wavenumber and s^* is the longitudinal coordinate taken to coincide with the coordinate of the channel axis. As seen in §2 (figure 4) the ratio of the channel width to the local radius of curvature of the channel
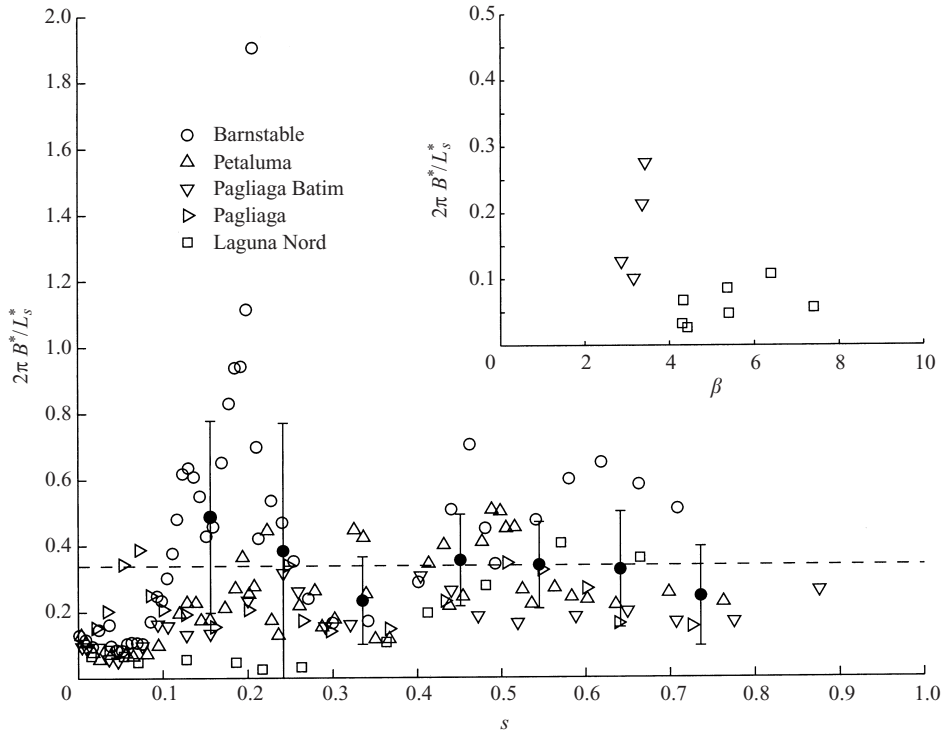
FIGURE 3. A collection of data from different tidal environments around the world (Barnstable (MA, USA), Petaluma (CA, USA), Pagliaga (Venice, Italy), described in detail in Fagherazzi *et al.* 1999 and Rinaldo et al. 1999*a*, *b*). Dimensionless ratio $2\pi B^*/L_s^*$ of width and intrinsic wavelength, plotted versus intrinsic distance $s = s^*/s_{max}^*$ (where s_{max}^* is the maximum distance from source to outlet for each meander) from the meander origin. Despite almost two orders of magnitude of width growth in the cases observed, and within rather different environments for tidal range, climate, geology or vegetation, the ratio remains remarkably constant in the range 0.2–0.4. Ensemble averages of binned data are also shown (filled circles) where a range of two variances has been computed as described in the text. Notice that small channels (say, for $s \leqslant 0.1$) suffer from inaccurate measurement of the small widths owing to the limitation of the topographic bases adopted. In the inset, width to depth ratio β is plotted against the relevant dimensionless wavelength in the few cases available as indicated by the legend.

axis is typically fairly small in estuarine environments, such that it is convenient to introduce the small parameter

$$\nu = \frac{B^*}{R_0^*}, \tag{3.2}$$

which will form the basis of a perturbation expansion of the solution derived in the next section. It is appropriate to refer flow and bed topography to the orthogonal curvilinear coordinate system (s^*, n^*, z^*) where s^* is the longitudinal coordinate defined previously, n^* is the coordinate of the transverse horizontal axis orthogonal to s^* and z^* is the usual vertical coordinate. Dependent and independent variables are scaled as in equations (2.2*a*–*f* I)† where x and y must be replaced by s and n respectively. Note that such a choice is appropriate to the present investigation which focuses on a channel reach of length equal to meander wavelength, which ranges typically about a few channel widths. With the above scaling and performing the useful coordinate

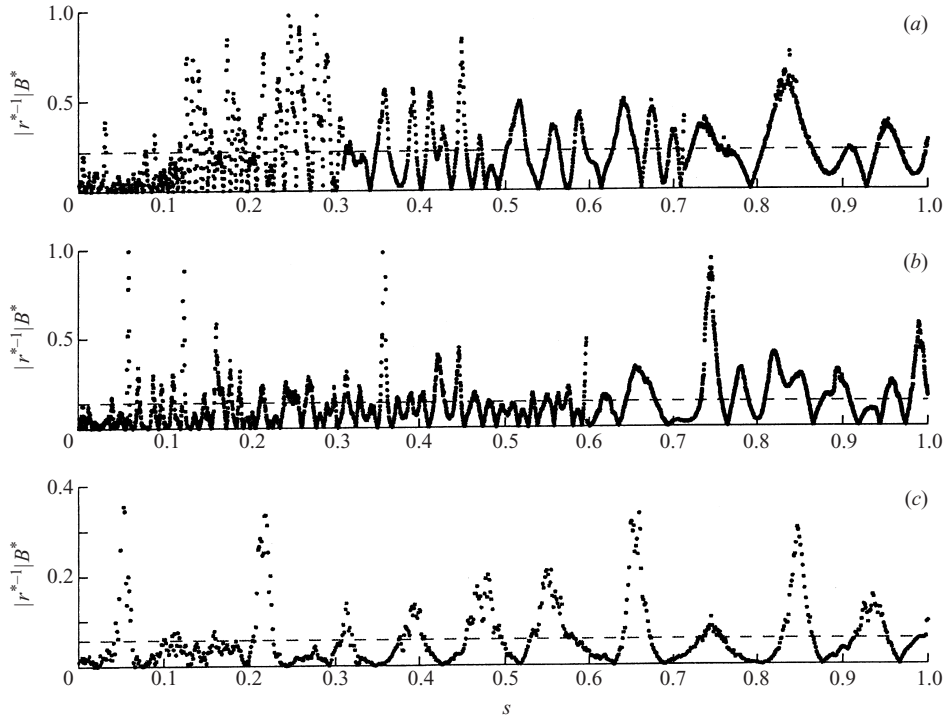† I denotes an equation number in Part 1.

FIGURE 4. Plot of the spatial development of the dimensionless product of local curvature and half-width, $r^{*-1}(s^*)B^*(s^*)$, for three tidal meanders of different size and geographic location: (*a*) Barnstable; (*b*) Petaluma, full set; (*c*) Petaluma, detailed subset. The dotted line shows the overall average: $\langle r^{*-1}B^* \rangle = 0.22$ (*a*); $= 0.14$ (*b*); $= 0.06$ (*c*). Notice that the largest fluctuations of the ratio may locally reach surprisingly high values, say close to unity.
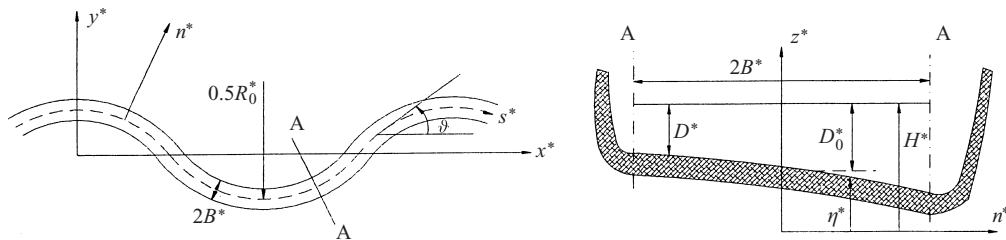

FIGURE 5. Sketch and notation.

transformation (2.16 I), the flow equations may be written in the form

$$LU = -\frac{N}{\mathscr{F}^2}\frac{\partial H}{\partial s} + \frac{\beta\sqrt{C_{f0}}}{D^2}\frac{\partial}{\partial Z}\left[v_T\frac{\partial U}{\partial Z}\right] - vc(s)NUV, \tag{3.3}$$

$$LV = -\frac{1}{\mathscr{F}^2}\frac{\partial H}{\partial n} + \frac{\beta\sqrt{C_{f0}}}{D^2}\frac{\partial}{\partial Z}\left[v_T\frac{\partial V}{\partial Z}\right] + vc(s)NU^2, \tag{3.4}$$

$$Nq_sU + [q_n + vNc(s)]V + \frac{1}{D}\frac{\partial W}{\partial Z} = 0, \tag{3.5}$$

where L is the partial differential operator

$$L \equiv \sigma_0 q_t + N U q_s + V q_n + \frac{W}{D} \frac{\partial}{\partial Z}, \tag{3.6}$$

and only the dominant Reynolds stresses have been retained in (3.3), (3.4). It is appropriate to point out at this stage that the sidewall boundary layers associated with the presence of the channel banks are excluded from the present analysis. This is known from the fluvial literature to be a convenient approximation for wide cross-sections with gently sloping banks. Furthermore σ_0 and q_j are the parameter and the operator defined by (2.8a I) and (2.28 I) respectively, while N^{-1} is the dimensionless form of the longitudinal metric coefficient:

$$N^{-1} = [1 + \nu n c(s)], \tag{3.7}$$

denoting by $c(s)$ the function which describes the spatial distribution of the dimensionless curvature B^*/r^*. Note that, just like in Part 1, the mean pressure is hydrostatically distributed and is

$$P = \frac{D}{\mathscr{F}^2}[1 - Z]. \tag{3.8}$$

Equations (3.3)–(3.5) must be solved along with the following boundary conditions:

$$U = V = W = 0 \quad (Z = Z_0), \tag{3.9}$$

$$[\sigma_0 q_t + N U q_s + V q_n] H - W = 0 \quad (Z = 1), \tag{3.10}$$

$$\frac{\partial V}{\partial Z} = \frac{\partial U}{\partial Z} = 0 \quad (Z = 1), \tag{3.11}$$

imposing the usual kinematic and dynamic constraints at the bed and at the free surface. At the channel banks, following the classical approach employed in the fluvial literature (which ignores the sidewall boundary layers, Engelund 1974 and Seminara & Tubino 1986) we impose the condition of vanishing transverse component of the water flux. This condition will be further clarified in the next section where the transverse component of the mean velocity will be decomposed into a centrifugally induced contribution characterized by vanishing depth average and a topographically induced contribution with non-vanishing depth average. As a consequence of the boundary condition at the channel banks, the latter component of the secondary flow must vanish. Hence

$$V = 0, \quad n = \pm 1. \tag{3.12}$$

The convection–diffusion equation is then written in the form

$$L\mathscr{C} - \beta \frac{W_s}{D} \frac{\partial \mathscr{C}}{\partial Z} = \frac{\beta \sqrt{C_{f0}}}{D^2} \frac{\partial}{\partial Z} \left(\psi \frac{\partial \mathscr{C}}{\partial Z} \right), \tag{3.13}$$

where we have neglected lateral and longitudinal diffusion which are $O(\beta^2)$ smaller than the vertical diffusion term, at least in the central region of the flow, as narrow channels and the sidewall boundary layers are excluded from the present analysis. Equation (3.13) must be solved with the following boundary conditions:

$$[(W_s \mathbf{k})\mathscr{C} + \sqrt{C_{f0}}\psi \nabla \mathscr{C}] \cdot \mathbf{n} = 0 \quad (Z = 1), \tag{3.14}$$

$$[(W_s \mathbf{k})\mathscr{C}_e + \sqrt{C_{f0}}\psi \nabla \mathscr{C}] \cdot \mathbf{n} = 0 \quad (Z = a_r), \tag{3.15}$$

	Barnst. 1	Barnst. 2	Barnst. 3	Pet. 1	Pet. 2	Pagl. 1	Pagl. 2	Pagl. 3
Mean of v	0.01	0.06	0.03	0.16	0.17	0.12	0.19	0.18
Max of v	0.05	0.30	0.23	0.64	1.14	1.05	1.27	1.26

TABLE 1. The mean and the maximum values of v for tidal meanders located in three distinct environments (Barnstable (MA, USA), Petaluma (CA, USA) and Pagliaga (Venezia, Italy)).

where the gradient operator and the velocity vector V are

$$\nabla = \left(\frac{N}{\beta} \mathrm{q}_s, \frac{1}{\beta} \mathrm{q}_n, \frac{1}{D} \frac{\partial}{\partial Z} \right), \quad V = \left(U, V, \frac{W}{\beta} \right). \tag{3.16}$$

Note that, in wide cross-sections the vertical velocity in the central region of the flow considered herein is $O(\beta)$ smaller than the lateral velocity, hence the scaling (3.16). At the sidewalls we must reinforce the condition that the n-components of both the fluid and the sediment fluxes must vanish.

Finally the bottom evolution equation in the present coordinate system is

$$\frac{\sigma_0}{\beta} \frac{\partial}{\partial t} \left[\mathscr{C}_M (H - D) + D \int_{a_r}^1 \mathscr{C} \mathrm{d}Z \right] + N \frac{\partial Q_s}{\partial s} + \left[\frac{\partial}{\partial n} + v c(s) N \right] Q_n = 0, \tag{3.17}$$

where $\mathscr{C}_M$ is the packing concentration of the granular bed, while Q_s and Q_n are the longitudinal and transverse components of the total sediment flux, defined in the form

$$(Q_s, Q_n) = Q_0 (Q_{bs}, Q_{bn}) + D \int_{a_r}^1 (U, V) \mathscr{C} \mathrm{d}Z. \tag{3.18}$$

Note that we are employing a different, though equivalent to (2.24 I), form of the sediment continuity equation. The differential systems (3.3)–(3.17), along with the closure relationships (2.15 I), (2.23 I), (3.8 I) and (5.1)–(5.6 I), form a closed set of equations which can be solved for arbitrary distributions of channel curvature once appropriate end conditions are assigned. In the following we will consider the periodic distribution (3.1) which is equivalent to the following form of the function $c(s)$:

$$c(s) = \exp(\mathrm{i}\lambda s) + \text{c.c.}, \tag{3.19}$$

where λ is the meander wavenumber scaled by B^{*-1}. As a result of such a choice, the end conditions will be simply replaced by periodicity conditions in space while initial conditions are replaced by periodicity conditions in time.

4. Linear solution for weakly meandering tidal channels

As discussed in Part 1, at the scale of bars, the unsteady basic flow can be taken as uniform in space at the leading order of approximation. Moreover, it is convenient at this stage to assume that the reference level for the vertical coordinate coincides with the average bottom elevation within the meander reach investigated herein. We then assume the channel to be weakly meandering, i.e. we set

$$v \ll 1. \tag{4.1}$$

Note that such a condition is appropriate to describe the typical meandering configurations observed in nature.

Table 1 shows the values of v calculated for each bend of the sequences corresponding to the tidal channels depicted in figure 2 (Barnstable 1, Petaluma 1, Pagliaga 1) and of some tributary channels (Barnstable 2 and 3, Petaluma 2, Pagliaga 2, 3) corresponding to different tidal environments. It appears that the average value of v ranges between 0.01 and 0.19. A linear theory of the type developed herein is thus generally appropriate to investigate fully developed natural meanders. It may also form the basis for an investigation of the formation of tidal meanders, based on a linear analysis of the planimetric instability of tidal channels as discussed in §6.

Taking advantage of this assumption we expand the solution in powers of the small parameter v in a neighbourhood of the basic state as follows:

$$(U, V, W, H, D) = (\bar{U}_0(t)F_0(Z), 0, 0, H_0(s), H_0(s)) + v(u, v, w, \mathscr{F}^2 h, d) + O(v^2), \quad (4.2)$$

where $H_0(s)$ is the free surface elevation associated with the basic tidal wave described in Part 1 (§3 and the Appendix); the perturbations u, v, w, h, d are functions of the independent variables s, n, Z, t and are also parametrically dependent on the slow spatial variable ξ describing the spatial distribution of the basic tidal motion (see Part 1, Appendix), though the latter dependence will not be considered herein. We emphasize that expansion (4.2) describes a forced solution of the morphodynamic problem, the forcing arising from the effect of channel curvature. In this respect the problem is substantially different from the 'free' problem treated in Part 1.

Similarly we expand the operators q_s, q_n, L and the eddy viscosity v_T in powers of v in the form

$$(q_s, q_n, L, v_T) = (q_{s0}, q_{n0}, \mathscr{L}_0, v_{T0}) + v(q_{s1}, q_{n1}, \mathscr{L}_1, v_{T1}) + O(v^2), \quad (4.3)$$

where

$$q_{s0} = \frac{\partial}{\partial s}, \qquad q_{n0} = \frac{\partial}{\partial n}, \qquad \mathscr{L}_0 = U_0 \frac{\partial}{\partial s}, \qquad v_{T0} = |\bar{U}_0(t)| \mathscr{N}(Z), \qquad (4.4a\text{–}d)$$

$$q_{s1} = \left[(1 - Z)\frac{\partial d}{\partial s} - \mathscr{F}^2 \frac{\partial h}{\partial s}\right] \frac{\partial}{\partial Z}, \qquad (4.5)$$

$$q_{n1} = \left[(1 - Z)\frac{\partial d}{\partial n} - \mathscr{F}^2 \frac{\partial h}{\partial n}\right] \frac{\partial}{\partial Z}, \qquad (4.6)$$

$$\mathscr{L}_1 = U_0 q_{s1} + (u - nc(s)U_0)q_{s0} + w\frac{\partial}{\partial Z} + v\frac{\partial}{\partial n}, \qquad (4.7)$$

$$v_{T1} = v_{T0}\left(d + \frac{\partial u/\partial Z}{\partial U_0/\partial Z}\bigg|_{Z_0}\right). \qquad (4.8)$$

Note that in equation (4.4a) local inertial effects have been neglected, an assumption justified by the smallness of parameter σ_0 (see discussion in Part 1, p. 54). The derivation of the expansion (4.8) is given in the Appendix. By substituting from (4.2)–(4.8) into the governing hydrodynamic equations (3.3)–(3.5) and the associated boundary conditions (3.9)–(3.11) and equating terms proportional to v^0 we recover the governing equation for the basic longitudinal velocity already discussed in Part 1, §3.

Proceeding to $O(v)$ we derive the linearized form of the differential problem gov-

erning the dynamics of flow perturbations as

$$\beta\sqrt{C_{f0}}\frac{\partial(\nu_{T0}(\partial u/\partial Z)}{\partial Z} - U_0\frac{\partial u}{\partial s} - \beta\sqrt{C_{f0}}\mathcal{N}(Z_0)|\bar{U}_0(t)\left|\frac{\partial u}{\partial Z}\right|_{Z_0}$$

$$= \frac{\partial h}{\partial s} - \frac{n}{\mathcal{F}^2}\frac{\partial H_0}{\partial s}c(s) + \frac{\partial U_0}{\partial Z}w - \beta C_{f0}\bar{U}_0(t)|\bar{U}_0(t)|d + U_0\frac{\partial U_0}{\partial Z}(1-Z)\frac{\partial d}{\partial s}, \quad (4.9)$$

$$\beta\sqrt{C_{f0}}\frac{\partial(\nu_{T0}(\partial v/\partial Z))}{\partial Z} - U_0\frac{\partial v}{\partial s} = \frac{\partial h}{\partial n} - c(s)U_0^2, \quad (4.10)$$

$$\frac{\partial u}{\partial s} + \frac{\partial v}{\partial n} + \frac{\partial w}{\partial Z} = -(1-Z)\frac{\partial U_0}{\partial Z}\frac{\partial d}{\partial s}, \quad (4.11)$$

$$u = v = w = 0 \quad (Z = Z_0), \quad (4.12a\text{--}c)$$

$$\frac{\partial u}{\partial Z} = \frac{\partial v}{\partial Z} = w = 0 \quad (Z = 1), \quad (4.13a\text{--}c)$$

having neglected terms of order $\mathcal{F}^2$ with respect to $O(1)$ terms. Also note that the bed of tidal channels is typically dune covered, hence variations of the friction coefficient are dominantly associated with variations of the Shields parameter (recall the discussion at the beginning of § 5 Part 1). Variations of the friction coefficient due to the effect of the small perturbation of flow depth, though formally of order v, are fairly small and have been neglected in (4.9), (4.10). This differential system can be solved by setting the following expansions:

$$(u, w, h, d) = \left\{(0, 0, \bar{h}n, \bar{d}n)\right.$$

$$\left. + \sum_{m=1}^{\infty}[u_m(Z,t), w_m(Z,t), h_m(t), d_m(t)]\sin Mn\right\}\exp(i\lambda s) + \text{c.c.}, \quad (4.14)$$

$$v = \left\{v_0(Z,t) + \left[\sum_{m=1}^{\infty}v_m(Z,t)\cos Mn\right]\right\}\exp(i\lambda s) + \text{c.c.}, \quad (4.15)$$

where $\bar{h}$ and $\bar{d}$ are parameters to be determined and M is the following parameter:

$$M \equiv \frac{\pi}{2}(2m-1) \quad (m = 1, 2, 3\ldots). \quad (4.16)$$

The structure of the above expansions arises as follows. If the channel had constant curvature and the flow were fully developed, only the zero depth-average contribution (*centrifugal contribution*) would arise in (4.14), (4.15): in this case no derivative in s appears in equations (4.9)–(4.11) and the secondary flow arises from the need to balance the difference between centrifugal forces (increasing in the vertical direction) and lateral pressure gradient (constant in the vertical direction). In a linear context this leads to lateral distributions of both flow depth and free surface elevation which are linear in the lateral coordinate n and to a lateral component of velocity which is independent of n (except for the sidewall boundary layers ignored in this analysis) and has vanishing depth average. This is the case treated in the fluvial environment by Engelund (1974) and later by several authors, including Kalkwijk & de Vriend (1980).

In the presence of longitudinal variations of channel curvature, a centrifugal contribution to secondary flow still exists, of course, but it cannot be self-balanced, unless the meander wavenumber is so small that the flow can be considered as fully developed at any cross-section. This is the first term appearing in (4.14), (4.15). However, a *topographic* component of the secondary flow with non-vanishing depth average now arises (the series in (4.14), (4.15)) to balance the equations. In fact the centrifugal term satisfies the *n*-component of the momentum equation exactly but it leaves the flow continuity equation and the *s*-momentum equation unbalanced (a topographic effect), hence the term $(\bar{d}n \exp(\mathrm{i}\lambda s))$ becomes a forcing term for both equations. The decomposition is useful, both mathematically because subtracting the centrifugal component leaves us with homogeneous conditions at the sidewalls (hence allowing the Fourier expansion of the remaining topographic component), and physically because it allows us to distinguish the two mechanisms (centrifugal versus topographic) controlling the establishment of a secondary flow and of the perturbed bottom topography.

Note that such a decomposition is similar to that proposed originally by Kalkwijk & de Vriend (1980) in the fluvial case, though they assumed a vertical structure of the topographic component of the secondary flow, which is not assumed but formally derived here.

The problem for v_0 is readily solved in the form

$$v_0 = |\bar{U}_0(t)|\mathscr{G}(Z\,;I), \tag{4.17}$$

$$\bar{h} = \bar{U}_0^2(t)\mathscr{H}, \tag{4.18}$$

where I is defined in (4.9c I) and the function $\mathscr{G}$ is the solution of the ordinary differential problem

$$\mathrm{L}_1\mathscr{G} = -\frac{1}{\beta\sqrt{C_{f0}}}[-\mathscr{H} + F_0^2(Z)], \tag{4.19}$$

$$\mathscr{G} = 0 \quad (Z = Z_0), \tag{4.20}$$

$$\frac{\partial\mathscr{G}}{\partial Z} = 0 \quad (Z = 1). \tag{4.21}$$

Moreover the operator L_1 is defined by (4.8 I), while the constant $\mathscr{H}$ is obtained by requiring that the solution for $\mathscr{G}$ satisfies the following integral condition:

$$\int_{Z_0}^1 \mathscr{G}(Z)\mathrm{d}Z = 0. \tag{4.22}$$

This condition reinforces the constraint of vanishing flux through the sidewalls. The system (4.19)–(4.21) is readily solved by shooting techniques. Note that (4.17) suggests that the centrifugally induced component of the secondary flow is identical in the flood and ebb phases. This is not surprising as the symmetry of the geometric configuration and of the basic longitudinal flow implies that the driving forces are perfectly symmetrical both in space and in time. The nonlinearity of the temporal dependence of the driving force is responsible for the generation of a nonlinear response of the secondary flow which emerges both in (4.17) and in (4.18). Residual terms are associated with this nonlinear character and may be interpreted as though the response to the oscillatory basic state includes a steady component of 'fluvial'

type. Similarly the problem for $(v_m, h_m; m = 1, 2, 3, \ldots)$ is solved in the form

$$h_m = |\bar{U}_0(t)| \mathcal{H}_m, \tag{4.23}$$

$$v_m = \mu \mathcal{H}_m \mathcal{G}_m(Z; I), \tag{4.24}$$

with $\mathcal{H}_m$ functions of time to be determined and the functions $\mathcal{G}_m (m = 1, 2, 3, \ldots)$ solutions of the following ordinary differential problem (parametrically dependent on time):

$$L_1 \mathcal{G}_m = 1, \tag{4.25}$$

$$\mathcal{G}_m = 0 \quad (Z = Z_0), \tag{4.26}$$

$$\frac{\partial \mathcal{G}_m}{\partial Z} = 0 \quad (Z = 1), \tag{4.27}$$

with μ defined by (4.9*b* I). Again, the solution of (4.25)–(4.27) is obtained by a shooting technique.

Having determined v_0 and v_m we can proceed to express w_m in terms of u_m and v_m using the continuity equation (4.11). We find

$$w_m = M \int_{Z_0}^{Z} v_m(\xi) \mathrm{d}\xi - \mathrm{i}\lambda \int_{Z_0}^{Z} u_m(\xi) \mathrm{d}\xi - (A_m \bar{d} + d_m) \mathrm{i}\lambda \bar{U}_0(t)$$

$$\times \left[F_0(1 - Z) + \int_{Z_0}^{Z} F_0(\xi) \mathrm{d}\xi \right], \tag{4.28}$$

where $A_m (m = 1, 2, 3, \ldots)$ are constants

$$A_m = -(-1)^m \frac{2}{M^2}. \tag{4.29}$$

We may then derive the differential equation for u_m by substituting from (4.14), (4.15) into (4.9) and using the structure of the solution obtained for the secondary flow. With the help of some algebraic manipulations and of the following definition:

$$f = \int_{Z_0}^{Z} u_m \mathrm{d}\xi, \tag{4.30}$$

we eventually derive the following structure of the solution for the function f:

$$f = \sum_{j=1}^{3} \varphi_j \phi_j, \tag{4.31}$$

with

$$\phi_j = \left(f_j - \frac{\partial^2 f_j / \partial Z^2}{\partial^2 f_0 / \partial Z^2} \bigg|_{Z=1} f_0 \right) \quad (j = 1, 2, 3), \tag{4.32}$$

and the functions $\varphi_j (j = 1, 2, 3)$ are

$$\varphi_1 = \Lambda \left[A_m \mathcal{H} |\bar{U}_0(t)| + \mathcal{H}_m \right] - \sqrt{C_{f0}} \bar{U}_0(t)(A_m \bar{d} + d_m) + \sqrt{C_{f0}} \bar{U}_0(t) A_m, \tag{4.33}$$

$$\varphi_2 = -\Lambda |\bar{U}_0(t)| (A_m \bar{d} + d_m), \tag{4.34}$$

$$\varphi_3 = \frac{M^2}{\beta_0 \sqrt{C_{f0}}} I \mathcal{H}_m. \tag{4.35}$$

Moreover the functions $f_j (j = 0, 1, 2, 3)$ are solutions of the ordinary differential

problem (4.22)–(4.24 I) with $a_j (j = 0, 1, 2, 3)$ defined as follows:

$$a_0 = 0, \quad a_1 = 1, \quad a_2 = \frac{\mathrm{d}F_0}{\mathrm{d}Z} \int_{Z_0}^{Z} F_0(\xi)\mathrm{d}\xi, \quad a_3 = \frac{\mathrm{d}F_0}{\mathrm{d}Z}\Gamma \qquad (4.36a\text{–}d)$$

and

$$\Gamma = \int_{Z_0}^{Z} \mathscr{G}_m(\xi)\mathrm{d}\xi. \qquad (4.37)$$

We finally impose the kinematic condition at the free surface (4.13c) which, with the help of (4.24), (4.28)–(4.30) and some algebraic manipulations, eventually leads to the following relationship between the quantities $\mathscr{H}_m$ and d_m for each m:

$$\mathscr{H}_m = \bar{h}_1 |\bar{U}_0(t)|\mathscr{H} + \bar{h}_2 \bar{U}_0(t)(A_m \bar{d} + d_m) + \bar{h}_3 \bar{U}_0(t)A_m, \qquad (4.38)$$

where

$$\bar{h}_1 = \Lambda^2 \phi_1|_1 A_m \left[\Gamma \mu M - \Lambda^2 \phi_1|_1 - \Lambda \mu M I \phi_3|_1\right]^{-1}, \qquad (4.39)$$

$$\bar{h}_2 = \bar{h}_1 \left[1 - \sqrt{C_{f0}}\phi_1|_1 - \Lambda I \phi_2|_1\right]/(\Lambda \phi_1|_1 A_m), \qquad (4.40)$$

$$\bar{h}_3 = \bar{h}_1 \sqrt{C_{f0}}/(\Lambda A_m), \qquad (4.41)$$

having used the definitions (4.9a, c I), (4.34 I) for Λ, I and Γ.

The reader will note that, through the relationship (4.38), the whole solution for the flow perturbations is linearly related to the quantity $(A_m \bar{d} + d_m)(m = 1, 2, 3, \ldots)$. It is then convenient to express the solution for the velocity perturbations in the form

$$(u_m, v_m, w_m) = (\hat{u}_1, \hat{v}_1, \hat{w}_1) + (\hat{u}_2, \hat{v}_2, \hat{w}_2)(A_m \bar{d} + d_m) \quad (m = 1, 2, 3, \ldots), \qquad (4.42)$$

where $\hat{u}_i, \hat{v}_i, \hat{w}_i$ $(i = 1, 2)$ are functions of the independent variables Z and t. The structure (4.42) of the solution for (u_m, v_m, w_m) has a simple physical explanation. In fact, part of this solution $(\hat{u}_1, \hat{v}_1, \hat{w}_1)$ is independent of the development of bottom perturbations, being driven by the forcing effect of centrifugally driven longitudinal slope of the free surface (term proportional to $\mathscr{H}$ in (4.33)) and by the metric variation of the longitudinal slope (second term in the right-hand side of (4.9) which gives rise to the third term in the right-hand side of (4.33)). Part of the solution of (4.42) is induced by perturbations of bottom topography, either centrifugally driven (terms proportional to $\bar{d}$ in (4.33) and (4.34)) or due to shoaling effects (terms proportional to d_m in (4.33), (4.34), (4.35)). The as yet unknown quantities $\bar{d}$ and d_m will be determined below by imposing the constraints required by sediment continuity. Also note that the relationship (4.38) does not exhibit any discontinuity at the instant of flow reversal.

Let us finally proceed to calculate the perturbation of the concentration field. Hence, we set the following expansion for the concentration $\mathscr{C}$ and the eddy diffusivity ψ in powers of the small parameter v:

$$(\mathscr{C}, \psi) = (\mathscr{C}_0, \psi_0) + v \left\{\left[\sum_{m=1}^{\infty} (\mathscr{C}_m(Z, t), \psi_m(Z, t))\sin(Mn)\right]\exp(\mathrm{i}\lambda s) + \text{c.c.}\right\}, \qquad (4.43)$$

where $\mathscr{C}_0$ and ψ_0 are the basic concentration and diffusivity fields obtained in Part 1, §3. Note that the perturbation ψ_1 of eddy diffusivity is related to the perturbation of the flow field through a relationship identical with (4.4 I), namely

$$\psi_1 = \psi_0 \left(d + \frac{\partial u/\partial Z}{\partial U_0/\partial Z}\bigg|_{Z_0}\right). \qquad (4.44)$$

Expanding u and d according to (4.14) one readily derives from (4.44) expressions for the amplitude $\psi_m(Z, t)$ appearing in (4.43). By substituting from the expansion (4.43) into the governing equations (3.13)–(3.15), employing the expression (4.42) and equating terms $O(v)$ we obtain the following differential system:

$$L_3 \mathscr{C}_m = \omega_{01}(Z, t) + \omega_{02}(Z, t)(A_m \bar{d} + d_m), \tag{4.45}$$

$$\left[\Psi C_{m,z} + G \mathscr{C}_m \right]_{Z=1} = \omega_{11}(t) + \omega_{12}(t)(A_m \bar{d} + d_m), \tag{4.46}$$

$$\left[\Psi C_{m,z} \right]_{Z=a_r} = \omega_{21}(t) + \omega_{22}(t)(A_m \bar{d} + d_m). \tag{4.47}$$

Note that Ψ is a function describing the vertical distribution of eddy diffusivity at equilibrium defined in (2.23 I) and (5.4 I). The functions $\omega_{0i}(Z, t)$ in (4.45), $\omega_{1i}(t)$ in (4.46) and $\omega_{2i}(t)$ in (4.47) $(i = 1, 2)$ are obtained from the corresponding relationships (4.33 I) for Ω, (4.36 I) for Ω_1 and (4.39 I) for Ω_0 by replacing $\hat{u}$ and $\hat{w}$ by $\hat{u}_i / \bar{U}_0(t)$ and $\hat{w}_i / \bar{U}_0(t)$ respectively, G given by (3.17 I). Note that the effect of the centrifugally induced secondary flow is only indirectly present through the forcing effect of $\bar{d}$ in the system (4.45)–(4.47); no direct effect can be present as the term $v(\partial \mathscr{C}/\partial n)$ in the convection–diffusion equation only enters at $O(v^2)$. Also note that the boundary conditions (4.46), (4.47) account for the effect of perturbation of the reference concentration $\mathscr{C}_e$ due to perturbations of the Shields parameter θ and of the local flow depth D. Finally note that the decomposition (4.42) for the velocity field drives, through convective terms, an analogous decomposition of the forcing terms in (4.45)–(4.47) and, hence, of the solution, for $\mathscr{C}_m$. In fact the solution of the differential system (4.45)–(4.47) is readily obtained in the form

$$\mathscr{C}_m = \hat{\mathscr{C}}_1(Z, t) + \hat{\mathscr{C}}_2(Z, t)(A_m \bar{d} + d_m), \tag{4.48}$$

where the functions $\hat{\mathscr{C}}_1$ and $\hat{\mathscr{C}}_2$ are again obtained by shooting techniques.

Let us then linearize and solve the sediment continuity equation along with the boundary condition of vanishing sediment flux through the sidewalls. To this aim we substitute from the expansions (4.14), (4.15), (4.43) and the expressions (4.42), (4.48) into the relationships (3.17), (3.18). Some tedious algebraic work eventually leads to the solution for the as yet unknown function $\bar{d}$:

$$\bar{d} = -\frac{\beta \sqrt{\theta_0}}{r Q_0 \phi_{b0}} \left[|\bar{U}_0(t)| \int_{a_r}^{1} \mathscr{C}_0 \mathscr{G} \, dZ + Q_0 \phi_{b0} \left. \frac{\partial \mathscr{G}/\partial Z}{dF_0/dZ} \right|_{Z_0} \right]. \tag{4.49}$$

Finally the functions d_m $(m = 1, 2, 3, \ldots)$ satisfy the following equations:

$$\left(s_1 - \frac{r M^2}{\beta \sqrt{\theta_0}} \right) d_m = -(s_2 + s_1 A_m \bar{d}), \tag{4.50}$$

where

$$s_1 = i\lambda \left[\frac{1}{Q_0 \phi_{b0}} \left(\bar{U}_0(t) \int_{a_r}^{1} \hat{\mathscr{C}}_2 F_0 \, dZ + \bar{U}_0(t) \int_{a_r}^{1} \mathscr{C}_0 F_0 \, dZ + \int_{a_r}^{1} \mathscr{C}_0 \hat{u}_2 \, dZ \right) \right]$$

$$+ \left. \frac{2\phi_0(\partial \hat{u}_2/\partial Z)}{\bar{U}_0(t)(dF_0/dZ)} \right|_{Z_0} + \frac{r M^2}{\beta \sqrt{\theta_0}} |\bar{U}_0(t)| \bar{U}_0(t) \bar{h}_2$$

$$- \frac{M}{Q_0 \phi_{b0}} \int_{a_r}^{1} \mathscr{C}_0 \hat{v}_2 \, dZ - \left. \frac{M(\partial \hat{v}_2/\partial Z)}{|\bar{U}_0(t)| dF_0/dZ} \right|_{Z_0}, \tag{4.51}$$

$$s_2 = \mathrm{i}\lambda \left[\frac{1}{Q_0\phi_{b0}} \left(\bar{U}_0(t) \int_{a_r}^1 \hat{\mathscr{C}}_1 F_0 \mathrm{d}Z + \int_{a_r}^1 \mathscr{C}_0 \hat{u}_1 \mathrm{d}Z \right) \right] + \frac{2\phi_\theta(\partial\hat{u}_1/\partial Z)}{\bar{U}_0(t)(\mathrm{d}F_0/\mathrm{d}Z)}\Bigg|_{Z_0}$$

$$+ \frac{rM^2}{\beta\sqrt{\theta_0}} \bar{U}_0(t)(\bar{U}_0(t)\bar{h}_1\mathscr{H} + |\bar{U}_0(t)|A_m\bar{h}_3)$$

$$- \frac{M}{Q_0\phi_{b0}} \int_{a_r}^1 \mathscr{C}_0 \hat{v}_1 \mathrm{d}Z - \frac{M(\partial\hat{v}_1/\partial Z)}{|\bar{U}_0(t)|\mathrm{d}F_0/\mathrm{d}Z}\Bigg|_{Z_0}, \tag{4.52}$$

with ϕ_θ given by (4.48 I). Equation (4.50) is easily solved numerically. Once the quantities $\bar{d}$ and $d_m (m = 1, 2, 3, \ldots)$ are known, the whole solution for the flow and topography fields is completely determined. The reader will note that the complex nature of the function $\mathscr{G}$ in (4.49) and of coefficients s_1 and s_2 in (4.50) suggests that both the 'centrifugally induced' lateral deformation of the bed and the topographically induced component are out of phase relative to channel curvature. The temporal dependence of both components is nonlinearly related to the basic velocity field.

5. Results for the flow and topography fields

Before discussing the main results obtained in the present work we provide some information about typical values of physical parameters controlling the morphodynamics of tidal channels. Data concerning typical widths, curvature radii of the channel axis and flow depths have already been given in figures 2 and 3 referring to three distinct tidal environments. Typical amplitude of flow velocity and of friction coefficient C_{f0} are in the range $(0.5–1)\,\mathrm{m\,s}^{-1}$ and $(4–2.5)\times10^{-3}$ respectively; a typical grain size is about $0.1\,\mathrm{mm}$ corresponding to a settling velocity of $1\,\mathrm{cm\,s}^{-1}$ and a particle Reynolds number about 4 (Danish Hydraulic Institute 1990). Friction velocity then is about $(3–6)\,\mathrm{cm\,s}^{-1}$ while the peak Shields stress (see (3.16 I)) attains values around 0.6–1.5. Typical values of the peak reference concentration are then immediately calculated from (5.1a, b, c I) and are found to increase from 4.4×10^{-5} to 9.6×10^{-5} as the Shields stress increases from 0.6 to 1.5. Such values are experienced at a reference distance from the bed of about $(3–16)\,\mathrm{cm}$, the bed being covered with dunes characterized by peak amplitudes of the order of $(20–80)\,\mathrm{cm}$.

Let us now describe the procedure employed to obtain our results. The analysis has been carried out considering the simplest temporal distribution of tidal velocity, namely

$$\bar{U}_0(t) = \cos(t). \tag{5.1}$$

Any other temporal dependence would be readily incorporated in the present theory. In particular the common presence of tidal dissymmetry would only lead to an asymmetric pattern of scour and deposition in meander bends.

Flow resistance has been evaluated using Einstein's (1950) formula in the plane-bed regime and Engelund–Hansen's (1967) approach in the dune-covered bed; the basic flow field was then obtained from (3.1 I), (3.9 I). We calculated the basic concentration field by means of (3.18 I) having calculated the dimensional fall velocity W_s^* using (5.6 I).

Once the basic state was completely determined, we could then calculate the perturbation of the flow field and finally the bottom topography. All the differential systems were solved numerically using a Runge–Kutta scheme of fourth order while quadratures were performed using Simpon's rule. Figure 6(a, b) shows examples of
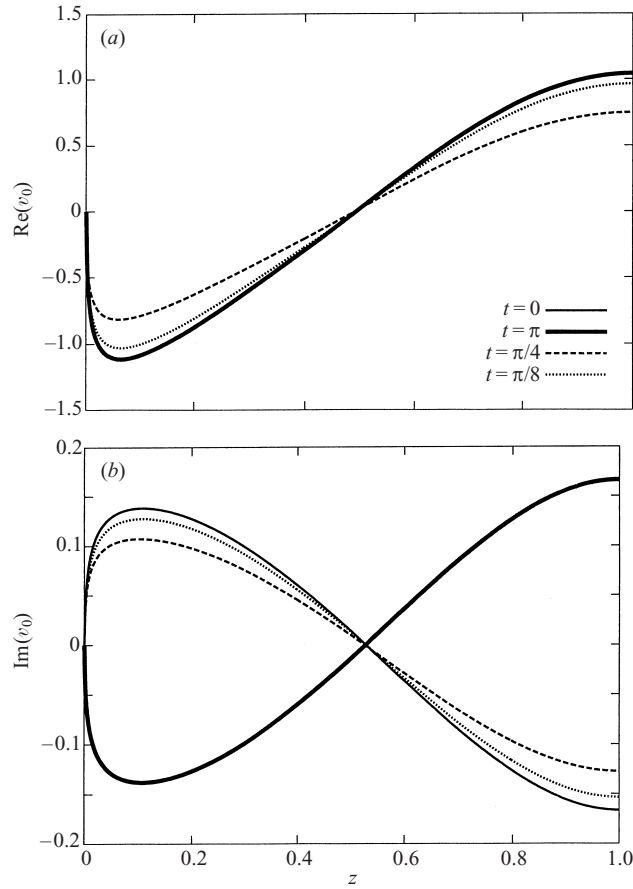
FIGURE 6. (*a*) The real part and (*b*) the imaginary part of the vertical distribution of the lateral component of velocity perturbation with vanishing depth average v_0 is plotted at various instants. (Values of the relevant parameters are $\beta = 6$, $\lambda = 0.05$, $R_p = 4$, $\bar{\theta}_0 = 0.6$, $d_s = 2 \times 10^{-5}$.)

the real part and imaginary part of the vertical distributions of the centrifugally induced lateral component of the perturbation velocity v_0 for given values of the relevant parameters β, C_{f0}, R_p, d_s at various instants during the tidal cycle, namely at the flood ($t = 0$) and ebb ($t = \pi$) peaks, as well as at $t = \pi/8, t = \pi/4$. The vertical distribution of the topographic component of the perturbation of the lateral velocity v_m for ($m = 1$) is plotted in figure 7(a, b). As one may expect from the symmetry of the problem it appears that the reversal of the basic tidal flow does not affect the secondary flow. Therefore the solutions for v_0 and v_m ($m = 1, 2, 3, \ldots$) satisfy the condition

$$v_m(Z, t) = \tilde{v}_m(Z, t + \pi) \quad (m = 0, 1, 2, 3, \ldots), \tag{5.2}$$

where a tilde denotes the complex conjugate of a complex number. Note that for the values of relevant parameters of figures 6(a, b), 7(a, b), 8(a, b), 9(a, b) the lateral component of secondary flow attains peak values equal to $2.7v V_0$. Figure 8(a, b) show the vertical distribution of the perturbation of the longitudinal velocity u_m for $m = 1$. Note that, due to the symmetry of channel geometry, the reversal of the basic flow leads to an antisymmetric pattern of the perturbation of the longitudinal velocity,
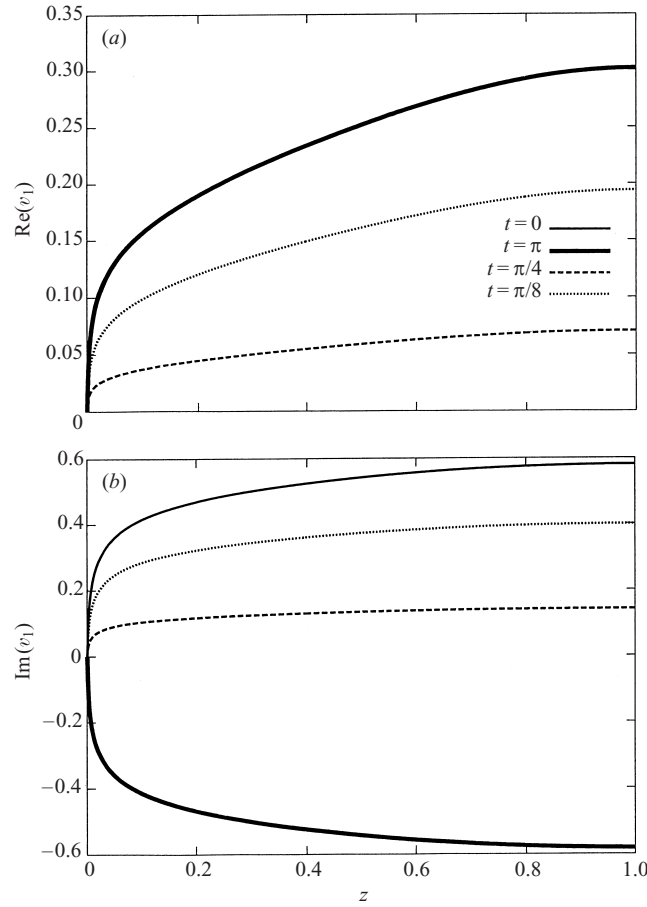
FIGURE 7. (*a*) The real part and (*b*) the imaginary part of the vertical distribution of the topographically driven lateral component of velocity perturbation $v_m(m = 1)$ is plotted at various instants. (The values of the relevant parameters are the same as in figure 6.)

hence

$$u_m(Z, t) = -\tilde{u}_m(Z, t + \pi) \quad (m = 1, 2, 3, \ldots). \tag{5.3}$$

Results for the vertical component of flow perturbation w_m ($m = 1$) (figure 9*a*, *b*) and for the perturbation of the sediment concentration $\mathscr{C}_1$ (figure 10*b*, *c*) display characteristics similar to those found for the lateral component of velocity perturbation. Note that, for the values of the relevant parameters of figure 10(*b*, *c*), $\mathscr{C}_1$ takes values of the same order as $\mathscr{C}_0$ which is plotted in figure 10(*a*).

Having determined the perturbation of the flow field, we then proceeded to evaluate the functions $\bar{d}(t)$ and $d_m(t)$ in order to obtain the pattern of bottom topography. Figure 11 shows the patterns of deposition and scour for given values of the relevant parameters at the positive ($t = 0$) and negative ($t = \pi$) peaks of the tidal cycle (the arrow indicates the direction of the basic flow). Again note the symmetrical position of the point bar–pool with respect to the bend apex, a result which provides a check of consistency for the present analysis. The patterns of the dimensionless velocity at the free surface (*a*) and of the dimensionless bed shear stress vector (*b*)
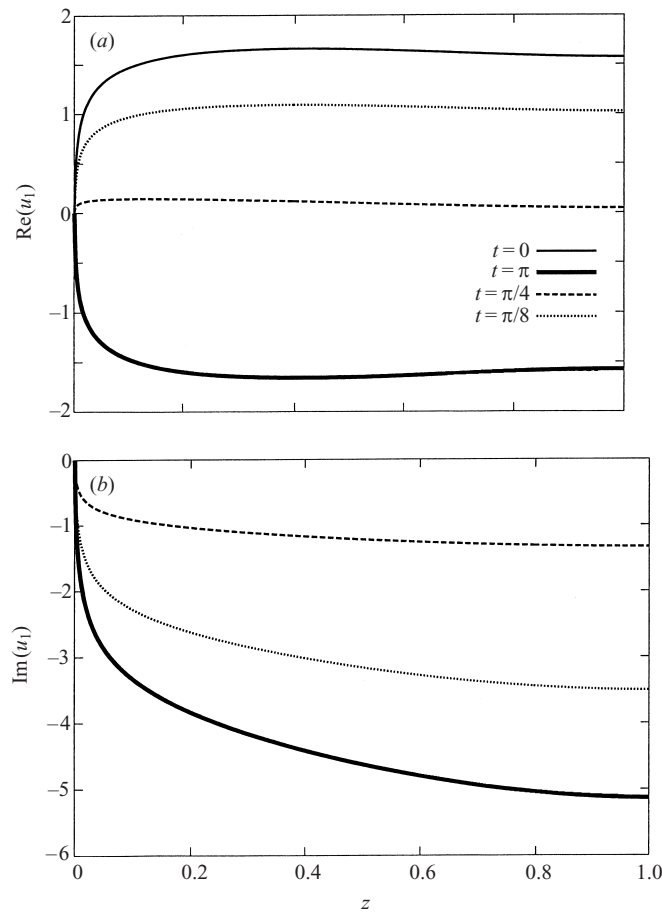
FIGURE 8. (*a*) The real part and (*b*) the imaginary part of the vertical distribution of the longitudinal flow perturbation $u_m(m = 1)$ is plotted at various instants. (The values of the relevant parameters are the same as in figure 6.)

are plotted in figure 12(*a*–*c*) at $t = 0, \pi/8, \pi/4$ respectively. As one may expect the thread of high-velocity shifts from the inner to the outer bend due to the effect of secondary flow, while the channel deepens towards the outer part of the bend. At the same time the channel experiences higher bed shear stress at the outer bank close to and downstream of the bend apex, thus indicating the tendency of the meander to amplify and migrate downstream. Note that, at each cross-section the transverse slope of the bottom is maintained through a balance, acting on bedload particles, between the inward transverse component of the bed shear stress and the outward downhill component of gravity. Such effects tend to weaken as the basic flow reversal is approached. Due to the periodicity of the basic flow, the point bar–pool pattern migrates alternately forward and backward in a symmetric fashion: in other words no net bar migration in a tidal cycle occurs. During the cycle the instantaneous Shields parameter varies from zero to some maximum value at the tidal peak. As the Shields parameter θ increases, sediment is transported at first as bedload; for larger values of θ suspension becomes an appreciable fraction of the total transport. At the same time the bottom surface experiences the formation of dunes ascertained by using van Rijn's (1984) criterion, according to which dunes are present whenever the stage
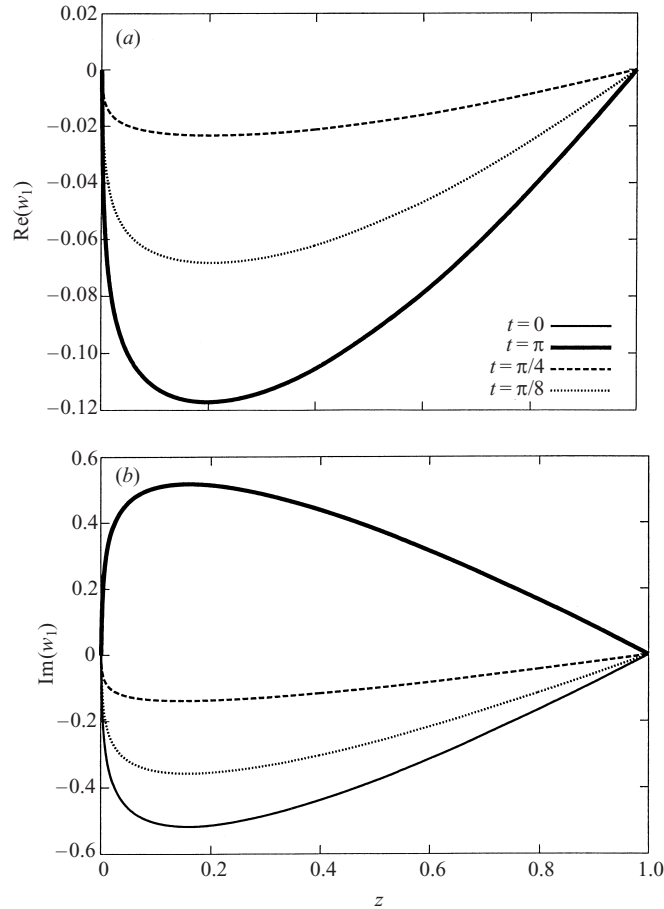
FIGURE 9. (*a*) The real part and (*b*) the imaginary part of the vertical distribution of the vertical flow perturbation $w_m(m = 1)$ is plotted at various instants. (The values of the relevant parameters are the same as in figure 6.)

parameter $(\theta' - \theta_c)/\theta_c$ is lower than 25. The oscillatory character of both the position and amplitude of the point bar emerges from figure 13(*a*) which shows the position and intensity of the maximum dimensionless flow depth during a quarter of a tidal cycle: $\Psi_{D_{max}}$ denotes the phase of the location where the maximum dimensionless flow depth D_{max} occurs at the outer bank, measured relative to the bend apex. Note that the location of the maximum scour oscillates in time with maximum displacement (in half a cycle) of the order of a fraction of a radian, hence a small value relative to meander wavelength. It appears that, as the intensity of the basic flow decreases, the point bar migrates upstream, decreasing its amplitude. Approaching basic flow reversal, the Shields parameter reaches some threshold value below which part of the channel cross-section becomes inactive: in other words, close to the inner bend the flow velocity can be so small that the Shields number falls below the threshold value for sediment motion. The analysis of Seminara & Solari (1998) suggests that the present approach fails when the mean Shields parameter is about 2–3 times θ_c, which corresponds to the minimum Shields parameter for the occurrence of transport throughout the whole of the cross-section. Note that overtides would not produce any net migration of point bars. This is clearly shown in figure 13(*b*) where we have
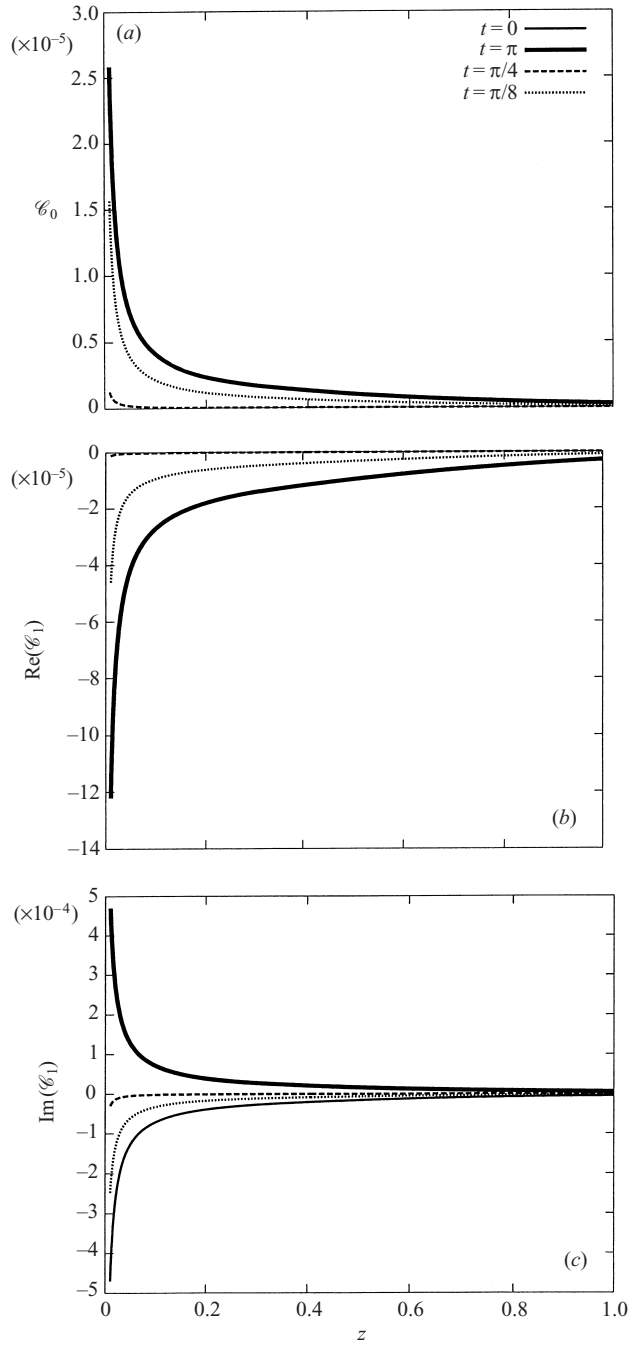
FIGURE 10. (*a*) The vertical distribution of the basic concentration field $\mathscr{C}_0$ is plotted at various instants. (*b*) The real part and (*c*) the imaginary part of the vertical distribution of perturbation of concentration field $\mathscr{C}_m$ ($m = 1$) is plotted at various instants. (The values of the relevant parameters are the same as in figure 6.)

plotted the location of the maximum dimensionless flow depth referred to a basic state characterized by the presence of a second harmonic, namely $\bar{U}_0(t) = \cos(t) + \frac{1}{5}\cos(2t)$. The figure clearly shows that this location oscillates back and forth in a perfectly symmetric fashion. The role of the suspension can be inferred from figure 14, which shows the amplitude of the maximum flow depth at $t = 0$ as a function of particle Reynolds number R_p, which controls the ratio of suspended to bedload (see the line labelled $q_{s0}/Q_0\phi_{b0}$). As has been shown by Seminara & Tubino (1986) in the fluvial case, suspension leads both to downstream shifting and to increasing amplitude of the point bar with respect to the case of vanishing suspended load, whereas flattening of the point bar occurs for higher values of the above ratio.

6. The formation of tidal meanders: a 'bend' process?

The above solution for the flow and bed topography fields can be set at the basis of a linear 'bend' instability theory of the type originally proposed by Ikeda *et al.* (1981) and later developed by Blondeaux & Seminara (1985).

The bend instability theory is best formulated in terms of a planimetric evolution equation of the meandering channel, a linear intrinsic form of which is readily obtained. Let $\hat{\zeta}$ denote the lateral migration rate of the channel, scaled by the quantity V_0, i.e. by the flow velocity scale (see (2.2c I)). Furthermore let s be the curvilinear coordinate which identifies the location at time t of the cross-section which was located at s_0 initially, the quantities s and t being dimensionless. The migration rate is a function of s and t through its dependence on the spatial and temporal distributions of the bank erosion rate. We will need to formulate some physically based closure assumption in order to couple the evaluation of $\hat{\zeta}$ to knowledge of the flow field, of bed topography and of the geological texture of the bank. Figure 15 shows that the relative displacement of two neighbouring points on the channel axis, say s and $s+ds$, in the infinitesimal time interval dt can be expressed in terms of the infinitesimal temporal variation of the angle ϑ which the tangent to the channel axis forms with some Cartesian direction x (say the valley axis). It is found that

$$\frac{\partial \hat{\zeta}}{\partial s} ds\, dt = \left(\frac{\partial \vartheta}{\partial t}\bigg|_{s_0} dt \right) ds. \tag{6.1}$$

Strictly speaking, the time derivative is a Lagrangian derivative. However, in the context of a linear stability theory, where deviations of the shape of the channel axis from the straight configuration are assumed to remain small, we may safely approximate the Lagrangian derivative by its Eulerian counterpart. Hence, the linear form of the planimetric evolution equation of the channel is

$$\frac{\partial \vartheta}{\partial t} = \frac{\partial \hat{\zeta}}{\partial s}. \tag{6.2}$$

The nonlinear version of (6.2) for the fluvial case is derived by Seminara *et al.* 2001 and has an integro-differential form. Meanders typically develop as a result of erosion at concave banks and deposition at the convex banks. This is a highly complex process which proceeds in an intermittent fashion: bank collapse may arise from excess scour at the bank toe, the development of tension cracks, the effects of ground water seepage and of vegetation, etc. However it has proved quite satisfactory (Ikeda *et al.* 1981; Mosselman 1991; Hasegawa 1989) to model the long-term meander development as a continuous process such that the lateral migration rate of the
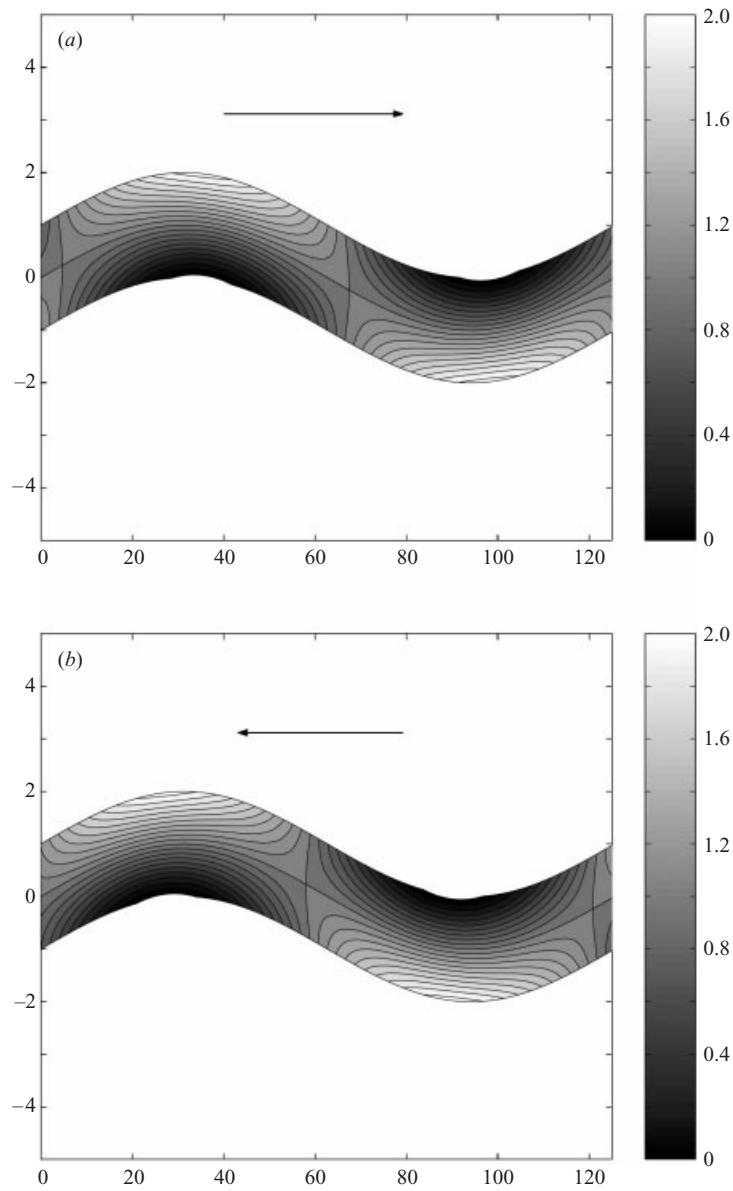
FIGURE 11. The pattern of the dimensionless flow depth is plotted at (*a*) the positive ($t = 0$) peak of the tidal cycle and (*b*) the negative ($t = \pi$) peak of the tidal cycle. (The values of the relevant parameters are the same as in figure 6 and $v = 0.03$.)

channel is simply proportional, through some erodibility coefficient e (of the order of 10^{-7}), to some measure of the perturbation of the flow field relative to the straight configuration. We rule out any possible effect of laterally symmetric components of the flow perturbations on the erosion rate, on the grounds that such symmetric components would lead to channel widening producing no shift of the channel axis: hence any appropriate measure of flow perturbation must be expressed in terms of the difference between the value attained at the outer bank and the corresponding value at the inner bank.
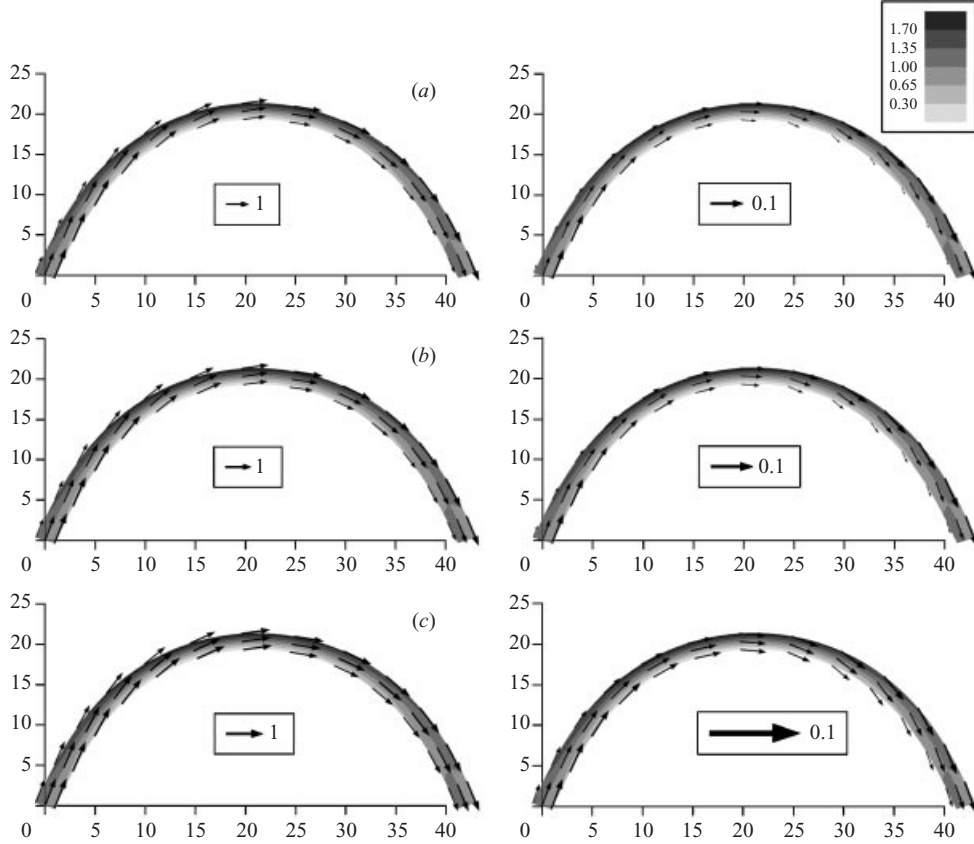
FIGURE 12. The pattern of the dimensionless velocity at the free surface (left) and of the dimensionless bed shear stress vector (right) is plotted at (*a*) the positive peak of the tidal cycle, (*b*) $t = \pi/8$ and (*c*) $t = \pi/4$. (The values of the relevant parameters are the same as in figure 6, and $v = 0.03$.)

We now assume that tidal meandering develops in a similar fashion as its fluvial counterpart. This assumption is tentatively based on the analogy between the plani-metric shapes of fluvial and tidal meanders but it does not rely on detailed field observations and will require substantiation in the near future. However, it is instruc-tive to analyse its implications. We propose a simple generalization of the erosion law suggested by Ikeda *et al.* (1981), accounting for the three dimensional and unsteady character of our flow field. In the context of the flow model employed by Ikeda *et al.* (1981), which was depth averaged and steady, the erosion law was assumed to be

$$\hat{\zeta} = ev(\tilde{U}|_{n=+1} - \tilde{U}|_{n=-1}), \qquad (6.3)$$

with $\tilde{U}$ perturbation of the longitudinal component of the depth-averaged velocity. In our case, we generalize (6.3) to account for the integrated effect of erosion throughout a tidal cycle. Hence we write

$$\hat{\zeta} = ev \left[\int_0^{2\pi} \left(\mathscr{I}_u|_{n=+1} - \mathscr{I}_u|_{n=-1} \right) dt \right], \qquad (6.4)$$

where $\hat{\zeta}$ represents the average lateral migration rate in a tidal cycle, where $\mathscr{I}_u = \int_{Z_0}^1 u \, d\xi$. Note that, in the context of a linear theory, different choices of the pertur-
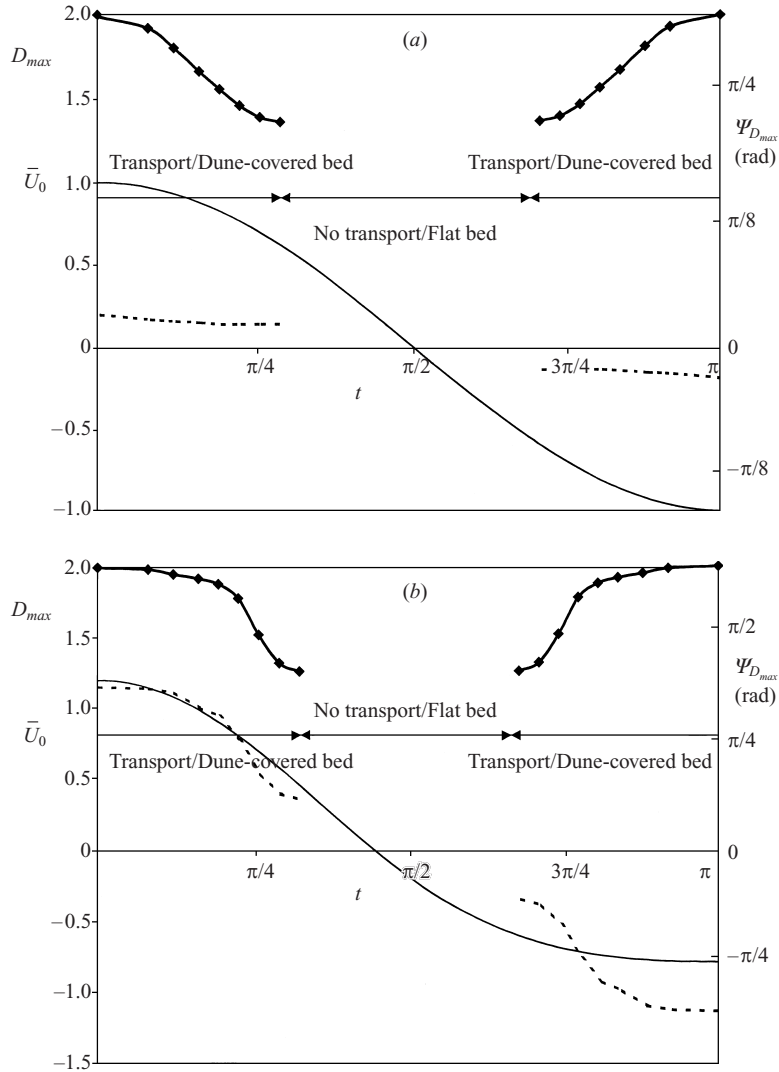
FIGURE 13. (*a*) Temporal variations of the position and intensity of the maximum dimensionless flow depth during half a tidal cycle. (The values of the relevant parameters are the same as in figure 6 and $v = 0.03$.) (*b*) Temporal variations of the position and intensity of the maximum dimensionless flow depth during half a tidal cycle in the case of a tidal velocity characterized by the following temporal distribution: $\bar{U}_0(t) = \cos(t) + \frac{1}{5}\cos(2t)$. (Values of the relevant parameters are $\beta = 5$, $\lambda = 0.1$, $R_p = 4$, $\bar{\theta}_0 = 1.6$, $d_s = 2 \times 10^{-5}$, $v = 0.02$.) The continuous line shows the temporal distribution of the basic flow field $|\bar{U}_0|$, the dashed lines show the phase lag between the cross-section where the maximum flow depth is located and the cross-section at the bend apex ($\Psi_{D_{max}}$), the bold continuous lines show the intensity of the maximum dimensionless flow depth (D_{max}).

bation quantity in (6.4) (say the perturbation of the bottom stress at the bank toe), would not lead to any significant differences in the predictions of the bend stability theory. We can then employ the solution derived in §4 to transform the planimetric evolution equation (6.2) with the closure assumption (6.4) into a linear amplitude equation for meander evolution. Recalling (3.1), (3.2) and noting that higher har-
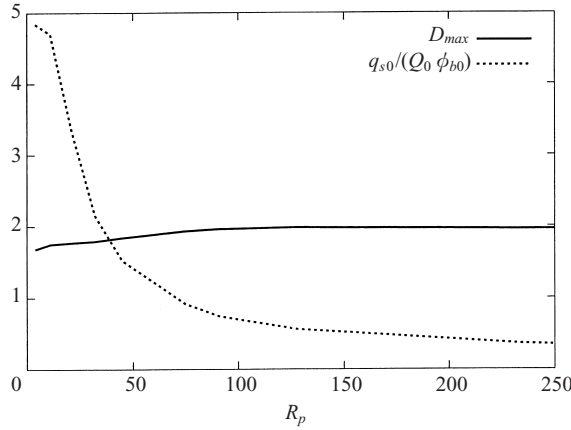
FIGURE 14. The amplitude of the maximum dimensionless flow depth is plotted as a function of R_p. (Values of the relevant parameters are $\beta = 5$, $\lambda = 0.25$, $\bar{\theta}_0 = 1.5$, $d_s = 10^{-4}$, $v = 0.03$.)
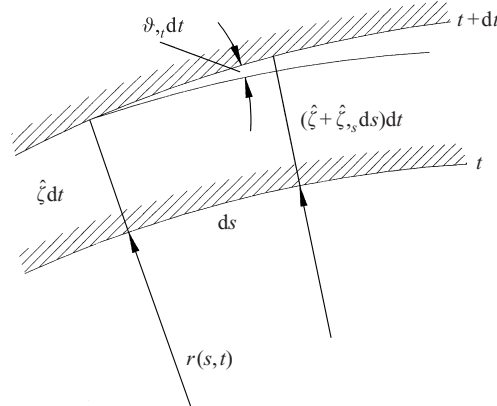

FIGURE 15. Planimetric evolution: sketch and notations.

monics are not generated as a result of a linear planimetric development, we may represent the instantaneous channel configuration as

$$\vartheta = \vartheta_0(t) \exp i\lambda s + \text{c.c.}, \tag{6.5}$$

where the function $\vartheta_0(t)$ plays the role of a meander amplitude. Comparison between this formulation and the definition (3.1) suggests that ϑ_0 is an imaginary number, hence it is convenient to set $\vartheta_0 = i\hat{\vartheta}_0$ with $\hat{\vartheta}_0$ real function such that

$$\hat{\vartheta}_0 = v/\lambda. \tag{6.6}$$

Recalling the expansion (4.14) and substituting from (6.4), (6.5) into the planimetric evolution equation (6.2) and using (6.6) we end up with the following amplitude equation:

$$\frac{\partial \hat{\vartheta}_0}{\partial t} = G\hat{\vartheta}_0, \tag{6.7}$$

where

$$G = \int_0^{2\pi} G_i \mathrm{d}t, \quad G_i = -2e\lambda^2 \left(\sum_{m=1}^{\infty} (-1)^m \mathscr{I}_{u_m} \right), \tag{6.8}$$

G_i being the instantaneous growth rate.

Not surprisingly, the amplitude equation (6.7) allows a simple exponential solution with complex growth rate G, a result typical of any linear stability theory. Hence, for given values of the width to depth ratio β, of the peak Shields parameter θ and of the particle Reynolds number R_p, meanders grow for values of the meander wavenumber λ such that the real part of the complex growth rate G is positive. Furthermore the net migration rate of the meander pattern is proportional to the imaginary part of G. The latter quantity is invariably found to vanish, confirming the absence of any net migration of the meander pattern, which could be anticipated on physical ground due to the absence of a preferential direction of the basic state. Figure 16 shows the typical trend exhibited by the growth rate as a function of meander wavenumber for given values of the relevant physical parameters. Such a trend is similar to that found in the river case (see, for instance, Blondeaux & Seminara 1985). It shows that initial perturbations with wavelength smaller than some threshold value decay. Moreover a peak of growth rate occurs for the most unstable wavenumber λ_m, depending on the flow and sediment parameters. Such peak is reminiscent of the analogous peak discovered by Blondeaux & Seminara (1985) for river meanders. This is not surprising as, in the context of the present formulation, the response of tidal meanders simply arises from an integrated effect of the instantaneous patterns associated with the oscillatory basic state. Hence the peak in the response is associated with the occurrence, during the tidal cycle, of resonant or quasi-resonant conditions in a similar fashion as found in the steady river case. Figure 17(a, b) shows the behaviour of the instantaneous growth rate G_i during a quarter of a tidal cycle. Each curve displays a maximum which may attain a large value, indicating that, for given values of the pair λ_m, β, the instantaneous Shields number θ is such that quasi-resonant conditions are typically approached. Resonance arises when curvature forces the flow–bottom topography under conditions such that the system allows a natural response in the form of non-amplifying and non-migrating bars with wavelength equal or close to the meander wavelength (see Part 1). The occurrence of resonance is displayed in figure 18 which shows that the topographically induced component of flow depth has an infinite peak at some value of the width ratio. Figure 19 shows the dependence of the most unstable wavenumber λ_m on the width to depth ratio β for various values of the peak value of the Shields parameter $\bar{\theta}_0$ and for given values of R_p and d_s. It appears that the wavenumber selected by the present planimetric instability analysis ranges between 0.02 and 0.15, at least for peak values of the Shields parameter greater than 0.6.

We cannot pursue a thoroughly satisfactory comparison between theory and experimental observations, as detailed measurements of the hydrodynamic and sedimentologic characteristics of tidal meanders are not available. However, observations reported in §2 suggest that the selected dimensionless wavenumbers are about 0.2–0.4, a range somewhat larger than that suggested by our figure 19, for typical values of the relevant physical parameters. Though we do not claim that the mechanisms which can possibly contribute to selecting the wavelengths of natural tidal meanders are wholly covered by our simplified formulation, the above comparison does support the idea that bend instability might be a mechanism leading to the formation of tidal meanders. Note that tidal meandering differs from river meandering for several reasons. One major feature is the oscillatory character of the basic state, which prevents meander migration. Moreover, as discussed in Part 1, free bars also exhibit no net migration in a tidal cycle. One might then argue that the planimetric instability of initially straight tidal channels is naturally forced by initial, finite-amplitude perturbations, consisting of free stationary bars. In other words, unlike the river case,
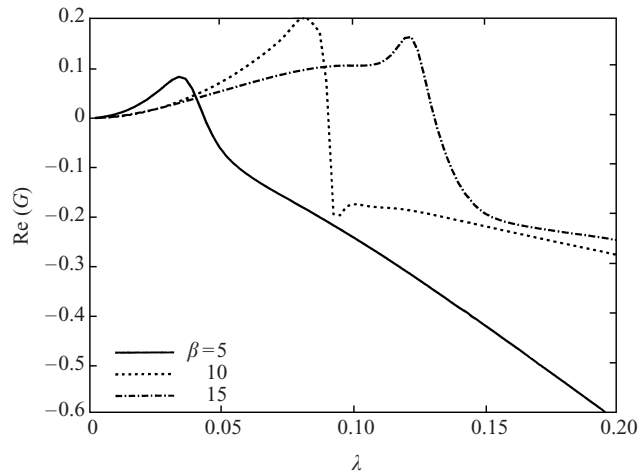
FIGURE 16. The real part of the complex growth rate of tidal meanders is plotted as a function of meander wavenumber λ and for given values of the width ratio β. (Values of the relevant parameters are $\bar{\theta}_0 = 1$, $d_s = 2 \times 10^{-5}$, $R_p = 4$.)

where free bars are migrating features, in the tidal case planimetric instability might not be a free instability but rather a process forced by the presence of stationary perturbations of the flow field and bottom topography in the straight configuration. This argument, however, has an intrinsic weak point: in fact, figure 19 shows that the wavenumber λ_b selected by the free bar mechanism is much larger than λ_c, the threshold value of meander wavenumber above which small-amplitude meandering perturbations are stable. Hence, free bars pre-existing in the straight channel cannot force the development of a meander pattern with their wavelength, as the latter do not amplify.

On the other hand, we are aware of another interesting observation: tidal meanders are typically more stable than river meanders. In other words their planimetric evolution is much slower than that of their fluvial counterparts. This may be partly due to the more cohesive character of channel banks, typically steeper than their fluvial counterparts. Furthermore the actual rate of lateral migration of river meanders is known to be controlled by the transport capacity of the stream, i.e. by its ability to remove the sediment accumulated at the bank toe. This capacity is rather stronger in the fluvial case, where the flow does not reverse, than in the tidal case. Furthermore, in tidal channels, vegetation growing in the adjacent salt marshes plays a stabilizing role which may alter the dynamics of tidal meanders.

The observation of tidal networks which have been stable for several decades (like Barnstable (MA, USA), Petaluma (CA, USA) and Pagliaga (Venice, Italy)), suggests the possibility that a process different from the type discussed in the present paper may be responsible for the formation of tidal meanders. The basic mechanism one may envisage can be simply described as follows: an initial incision cut in a purely cohesive tidal flat widens progressively till it reaches some equilibrium width slowly varying in the longitudinal direction. The widening process may be planimetrically unstable leading to meandering of the channel axis. This process may embed the meandering channel at some initial stage in the tidal network which may then be progressively stabilized by the growth of vegetation. This mechanism, which will have to be substantiated by an appropriate theoretical analysis, does not require
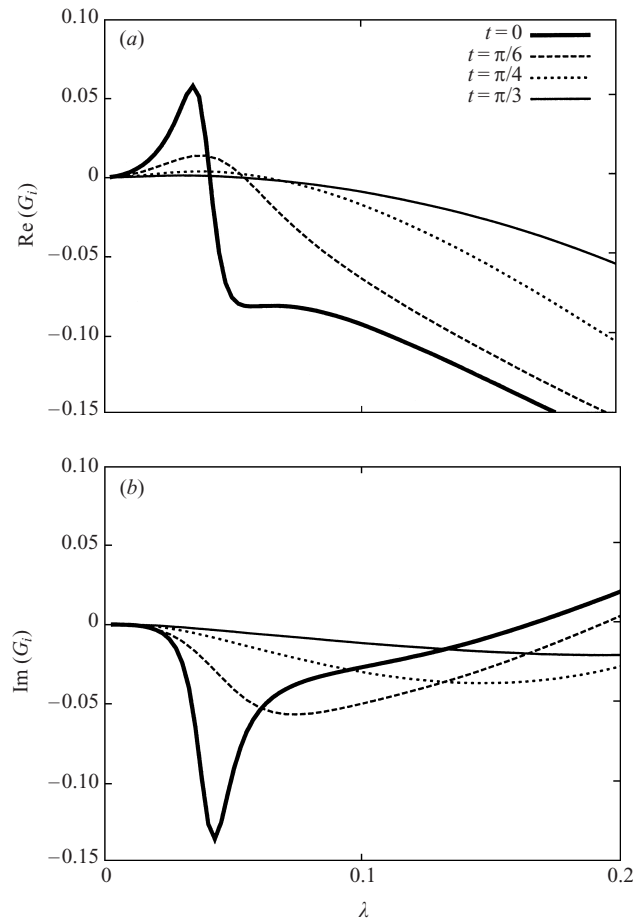
FIGURE 17. (*a*) The real part and (*b*) the imaginary part of the instantaneous complex growth rate of tidal meanders is plotted as a function of meander wavenumber λ for different values of the width ratio β. (Values of the relevant parameters are $\bar{\theta}_0 = 1$, $d_s = 2 \times 10^{-5}$, $R_p = 4$, $\beta = 5$.)

the assumption that the tidal stream has the ability to progressively shift the inner convex banks through the deposition of sediment eroded from the outer (concave) banks, a process known to occur in fluvial environments but not applicable to purely cohesive environments. We are currently investigating the feasibility of these latter ideas.

7. Concluding remarks

The field evidence reported in §2 suggests that the process of formation of tidal meanders displays a characteristic spatial scale in the range of about 10–15 channel widths. It is important to appreciate that this scale is found to be fairly uniform in channels whose width may change by two orders of magnitude. In other words the mechanism of meandering initiation is definitely controlled by morphodynamic effects acting at a scale of a few channel widths. This observation has motivated the present attempt to interpret the above process on the basis of a planimetric instability theory of the type established for fluvial meandering. The theoretical results discussed in
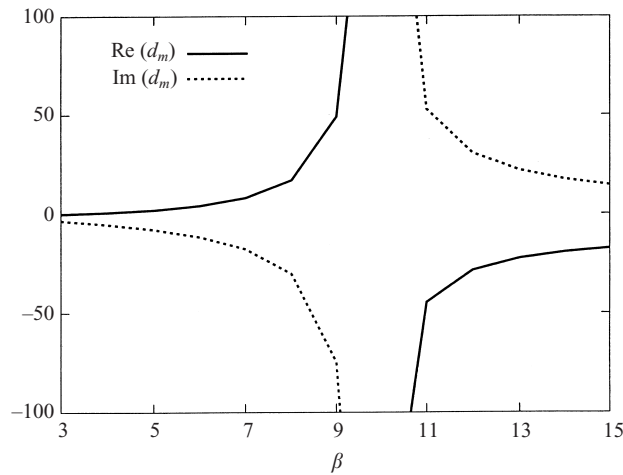
FIGURE 18. The values of topographically induced component of flow depth $d_m(m = 1)$ is plotted versus the width ratio β. (Values of the relevant parameters are $\bar{\theta}_0 = 0.6$, $\lambda = 0.09$, $d_s = 2 \times 10^{-5}$, $R_p = 4$.) Note the occurrence of a resonant peak.

the previous sections show that such a planimetric instability mechanism may indeed operate and selects meander wavenumbers of the correct order of magnitude, though somewhat smaller than those observed in nature.

Other simplifying assumptions adopted in the present work will require attention in the near future. Having neglected the contribution proportional to σ_0 in the bottom evolution equation (3.17) we have essentially assumed 'quasi-equilibrium', i.e. we have assumed that the bottom configuration adapts instantaneously to changes of the flow field throughout the tidal cycle. However, from a more careful examination, it turns out that this assumption is unduly severe and can be readily removed, as shown by Solari & Toffolon (2001). They have shown that, starting from an initial configuration characterized by a flat bed with a uniform flow depth along the channel, the system reaches an equilibrium topographic pattern such that throughout a tidal cycle the bottom displays relatively low-amplitude oscillations around a mean level which no longer changes in time. It is found that the system attains 'quasi-equilibrium' conditions only when two limiting cases are approached, namely when the tidal wave is so 'long' that the system is able to adapt instantaneously to the changing flow configuration or when transport in suspension is extremely 'strong'.

Furthermore, channel convergence may appreciably affect the structure of point bars induced by channel curvature. Also, sediments are often cohesive in the inner portion of tidal channels, a feature which has been ignored in the present analysis. Tidal flats adjacent to the main channel, besides producing a storage effect which controls the adjustment of channel width, may also affect the structure of point bars through their influence on the hydrodynamics of channel flow. The present theory is linear, in that perturbations induced by channel curvature are taken to be small enough. As meanders develop, both geometric and flow nonlinearities may become important, as well as nonlinear interactions between the free bars discussed in Part 1 and point bars analysed in the present paper. The inclusion of nonlinear effects will also allow an investigation of the important question of the occurrence of a net sediment flux driven by the presence of bars. A further source of nonlinearity arises in macrotidal environments whenever the amplitude parameter ϵ (see (2.1*a*
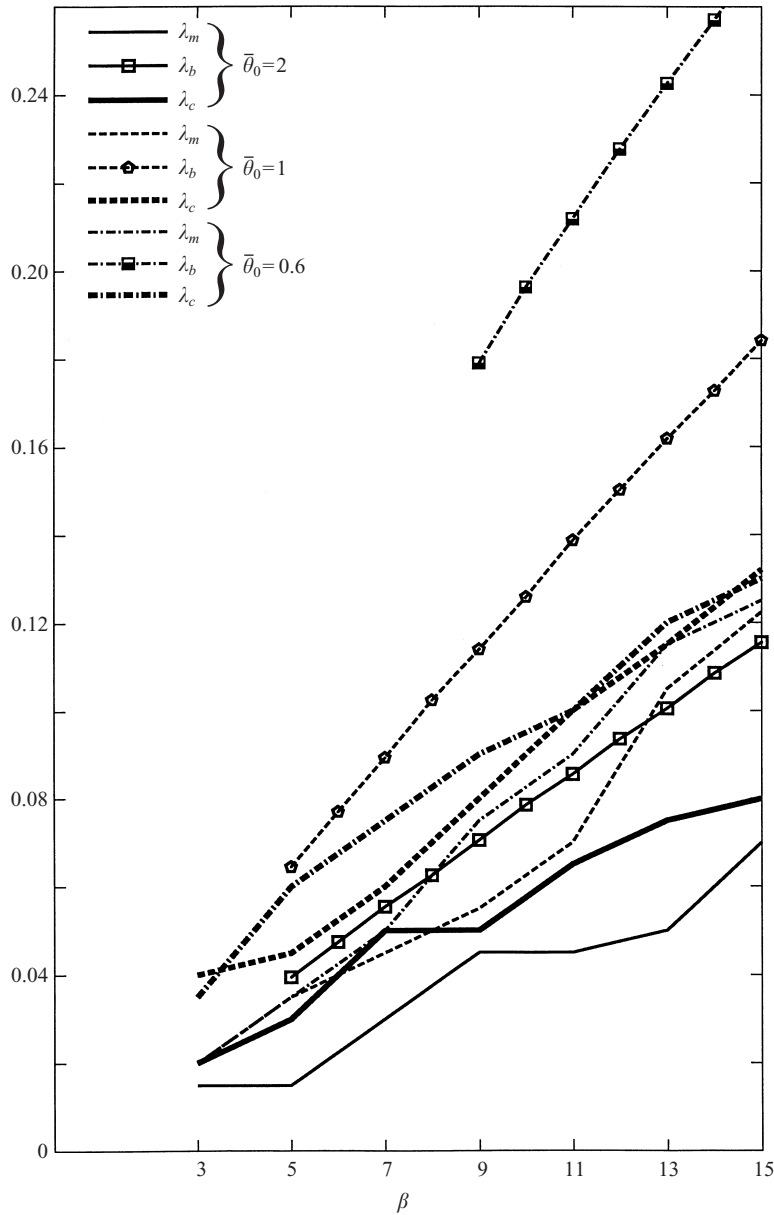
FIGURE 19. The values of meander wavenumber λ_m selected by bend instability, of meander wavenumber λ_c above which small-amplitude meandering perturbations are stable and of the wavenumber λ_b selected by the free bar mechanism (see Part 1, figure 10), are plotted versus the width ratio β for given values of the values of the peak value of the Shields parameter $\bar{\theta}_0$. (Values of the relevant parameters are $d_s = 2 \times 10^{-5}$, $R_p = 4$.)

I)) attains finite values. Under these conditions the topographic pattern driven by channel curvature displays a strong asymmetry

Detailed field observations of flow and bed topography in natural channels and of the role of vegetation in controlling the process of bank erosion are essential to further substantiate the present work. Progress in understanding the morphodynamics

of curved tidal channels will also benefit from detailed experimental observations performed in the laboratory. Finally, the approach employed in the present paper relies on a 'cohesionless mechanism' of channel shift similar to that known to be characteristic of fluvial environments. An alternative 'cohesive mechanism' appears to be possible and likely to be responsible for the formation of tidal meanders, as discussed at the end of the previous section.

Appendix. Linearization of the eddy viscosity coefficient

From (2.15 I) we have

$$v_T = u_* D \mathcal{N}(Z), \tag{A 1}$$

hence, expanding u_* and D in powers of v according to (4.2):

$$v_T = v_{T0} \left[1 + v \left(d + \frac{u_{*1}}{u_{*0}} \right) + O(v^2) \right]. \tag{A 2}$$

An expression for u_{*1}/u_{*0} is readily obtained from the definition

$$u_*^2 = \frac{T_{zs}^*|_{z_0^*}}{\rho V_0^2 C_{f0}}, \tag{A 3}$$

where the contribution of $T_{zn}^*|_{z_0^*}$ is ignored, being of order v^2. From (A 3) we find

$$u_*^2 = \frac{v_T^*(\partial U^*/\partial z^*)|_{z_0^*}}{V_0^2 C_{f0}} = v_T \left. \frac{\partial U}{\partial z} \right|_{z_0} = \frac{v_T}{D} \left. \frac{\partial U}{\partial Z} \right|_{Z_0}. \tag{A 4}$$

Hence, expanding both sides of equation (A 4) in powers of v yields

$$u_{*0}^2 \left(1 + 2v \frac{u_{*1}}{u_{*0}} + O(v^2) \right)$$
$$= v_{T0} \left(1 + v \frac{v_{T1}}{v_{T0}} + O(v^2) \right) (1 - vd + O(v^2)) \left(\left. \frac{\partial U_0}{\partial Z} \right|_{Z_0} + v \left. \frac{\partial u}{\partial Z} \right|_{Z_0} + O(v^2) \right). \tag{A 5}$$

Using (A 2) to express v_{T1}/v_{T0} in (A 5) and equating terms of various orders in v we finally find

$$O(v^0): \quad u_{*0}^2 = v_{T0} \left. \frac{\partial U_0}{\partial Z} \right|_{Z_0}, \tag{A 6}$$

$$O(v^1): \quad \frac{u_{*1}}{u_{*0}} = \frac{\partial u/\partial Z|_{Z_0}}{\partial U_0/\partial Z|_{Z_0}}. \tag{A 7}$$

Substituting from (A 7) into (A 2) we finally recover equation (4.8).

REFERENCES

ALLEN, J. R. L. & PYE, K. 1992 Coastal saltmarshes: their nature and importance. In *Saltmarshes – Morphodynamics, Conservation and Engineering Significance* (ed. J. R. L. Allen & K. Pye), pp. 1–18. Cambridge University Press.

BLONDEAUX, P. & SEMINARA, G. 1985 A unified bar-bend theory of river meanders. *J. Fluid Mech.* **157**, 449–470.

DANISH HYDRAULIC INSTITUTE 1990 Venice Lagoon–Study C.2.3: Morphological Field Investigations, Intensive measurements, Final report *Consorzio Venezia Nuova.*

EINSTEIN, H. A. 1950 The bedload function for sediment transport in open channel flow. *US Dept. Agric. Tech. Bull.* 1026.

ENGELUND, F. 1974 Flow and bed topography in channel bends *J. Hydraul. Div. ASCE* **100**(HY11), 1631–1648.

ENGELUND, F. & HANSEN, E. 1967 *A Monograph on Sediment Transport in Alluvial Streams.* Copenhagen: Danish Technical Press.

FAGHERAZZI, S., DIETRICH, W. E., ADAMI, A., LANZONI, S., MARANI, M. & RINALDO, A. 1999 Tidal networks 1. Automatic network extraction and preliminary scaling features from digital terrain maps. *Water Resour. Res.* **35**(12), 3891–3904.

FRENCH, J. R. & STODDARD, D. R. 1992 Hydrodynamics of salt marsh creek systems: implications for morphological development and material exchange. *Earth Surf. Proc. Landf.* **17**, 235–232.

HASEGAWA, K. 1989 *Study on Qualitative and Quantitative Prediction of Meander Channel Shift.* AGU Water Resources Monograph, vol. 12, pp. 215–235.

IKEDA, S. & PARKER, G. (Eds.) 1989 *River Meandering.* Water Resources Monograph, vol. 12, AGU, Washington DC.

IKEDA, S., PARKER, G. & SAWAI, K. 1981 Bend theory of river meanders. Part 1. Linear development. *J. Fluid Mech.* **112**, 363–377.

KALKWIJK, J. P. TH. & VRIEND, H. J. DE 1980 Computation of the flow in shallow river bends. *J. Hydraul. Res.* **18**, 327–342.

LANGBEIN, W. B. 1963 The hydraulic geometry of a shallow estuary. *IAHS J.* **8**, 84–94.

LANGBEIN, W. B. & LEOPOLD, L. B. 1964 Quasi-equilibrium states in channel morphology. *Am. J. Sci.* **262**, 782–794.

LEOPOLD, L. B. & WOLMAN, M. G. 1957 River channel patterns: braided, meandering and straight. *US Geol. Survey Prof.* 282-B.

MOSSELMAN, E. 1991 Modelling of the river morphology with non-orthogonal horizontal curvilinear coordinates. *Commun. Hydr. and Geotech. Engng* 91–1. Delft University of Technology, The Netherlands.

PESTRONG, R. 1965 *The Development of Drainage of Patterns on Tidal Marshes.* Stanford University Publications, Geological Sciences, vol. X.

RIJN, L. C. VAN 1984 Sediment transport, part II: suspended load transport. *J. Hydraul. Engng ASCE* **110**(11), 1613–1641.

RINALDO, A., FAGHERAZZI, S., LANZONI, S., MARANI, M. & DIETRICH, W. E. 1999a Tidal networks 2. Watershed delineation and comparative network morphology. *Water Resour. Res.* **35**(12), 3905–3917.

RINALDO, A., FAGHERAZZI, S., LANZONI, S., MARANI, M. & DIETRICH, W. E. 1999b Tidal networks 3. Landscape-forming discharges and studies in empirical geomorphic relationships. *Water Resour. Res.* **35**(12), 3919–3929.

ROZOVSKIJ, I. L. 1957 Flow of water in bends of open channels. Kiev: *Acad. Sci. Ukranian. SSR.*

SEKINE, M. & PARKER, G. 1992 Bed load transport on transverse slope – 1. *J. Hydraul. Engng ASCE* **118**(4), 513–535.

SEMINARA, G. & SOLARI, L. 1998 Finite amplitude bed deformations in totally and partially transporting wide channel bends. *Water Resour. Res.* **34**(6) 1585–1598.

SEMINARA, G. & TUBINO, M. 1986 Further results on the effect of transport in suspension on flow in weakly meandering channels. In *Colloquium on The Dynamics of Alluvial Rivers, 25–26 June 1986.* Hydraulic Institute, Genoa University, Italy.

SEMINARA, G. & TUBINO, M. 1992 Weakly nonlinear theory of regular meanders. *J. Fluid Mech.* **244**, 257–288.

SEMINARA, G. & TUBINO, M. 2001 Sand bars in tidal channels. Part 1. Free bars. *J. Fluid Mech.* **440**, 49–74.

SEMINARA, G., ZOLEZZI, G., TUBINO, M. & ZARDI, D. 2001 Downstream and upstream influence in river meandering. Part 2. Planimetric development. *J. Fluid Mech.* **438**, 213–230.

SOLARI, L. & TOFFOLON, M. 2001 Equilibrium bottom topography in tidal meandering channels: preliminary results. In *IAHR Symposium on River, Coastal and Estuarine Morphodynamics, Obihiro, Japan, 10–14 September 2001.*

STEEL, T. J. & PYE, K. 1997 The development of saltmarsh tidal creek networks: Evidence from the UK. *Proc. 1997 Canadian Coastal Conference*, vol. 1, pp. 267–280.

STRUIKSMA, N., OLESEN, K. W., FLOKSTRA, C. & VRIEND, H. J. DE 1985 Bed formation in curved alluvial channels. *J. Hydraul. Res.* **23**, 57–79.

TALMON, A. M., MIERLO, M. C. L. M. VAN & STRUISKMA, 1995 Laboratory measurements of the direction of sediment transport on transverse alluvial-bed slopes. *J. Hydraul. Res.* **33**, 495–517.

ZANDOLIN, D. 1999 Morphological analysis of tidal networks. Dr.Ing. dissertation, University of Padua (in Italian).